Volume 25
Number 20
21 October 2025
Pages 5105–5396

Lab on a Chip

Devices and applications at the micro- and nanoscale

rsc.li/loc

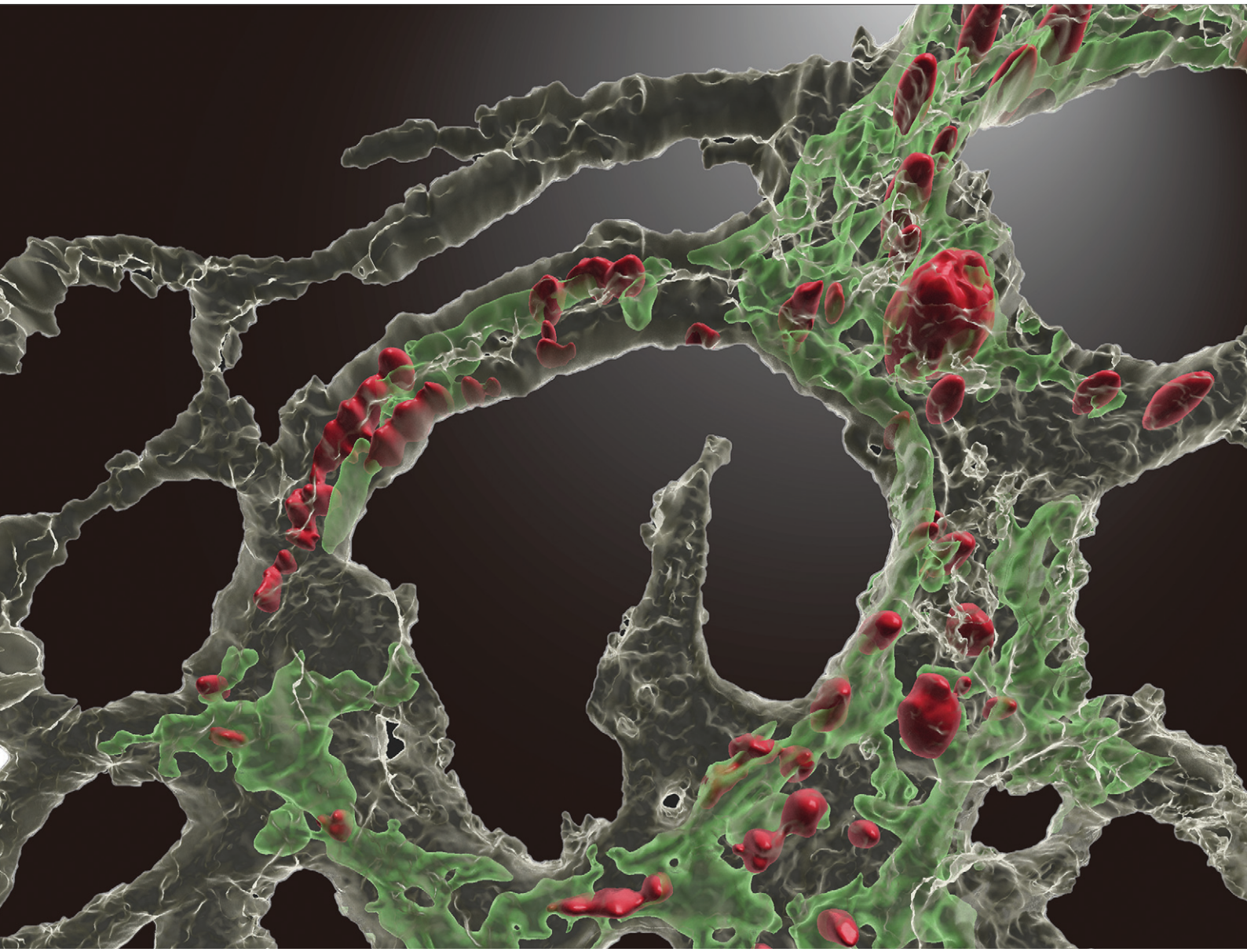

ISSN 1473-0197

ROYAL SOCIETY OF CHEMISTRY

PAPER

Yu-Hsiang Hsu *et al.*

Self-assembled human arteriole-on-a-chip for arterial functionality testing and disease modeling

Lab on a Chip

PAPER

View Article Online
View Journal | View Issue

Check for updates

Cite this: *Lab Chip*, 2025, **25**, 5162

Self-assembled human arteriole-on-a-chip for arterial functionality testing and disease modeling†

Subhashree Shivani,[a] Hsin-Jou Wang,[b] Yi-Ting Chen,[b] Chih-Ting Lin[a] and Yu-Hsiang Hsu *[bc]

In recent years, various vascularized organ-on-a-chip models have been designed for drug development and screening, and many of them have also advanced to serve as disease models for studying infectious diseases and gene disorders. Currently, most vascular models are capillary-like structures with only a layer of endothelium. Some of them may have pericytes to support the vessel structure. However, there are very limited studies on developing the complex structure of the arteries. In this study, we report a physiological approach to develop self-assembled arterioles in a microfluidic device, providing an *in vitro* model for human arterioles. First, we use human umbilical artery endothelial cells (HUAECs) and smooth muscle cells (HUSMCs) to create a vessel network through vasculogenesis and angiogenesis. Then, a 1 Hz oscillating pressure is applied to create two different levels of wall shear stress on the vessel network to stimulate arteriogenesis. Using this method, self-assembled arterioles are successfully developed in a microfluidic chip with HUAEC endothelium wrapped by HUSMCs and a basement membrane. The experimental studies show that vessel networks under high shear stress tend to grow over time. Furthermore, the concurrent formation of primary vessels with enlarging diameters and regression of secondary vessels with thinning diameters can be observed, suggesting that cyclic shear flow is a critical physiological stimulus in arteriole development. Finally, we verified the functionality of the developed arterioles. Vasodilation and vasoconstriction can be stimulated by administering varying dopamine concentrations into the arteriole chip, suggesting they are functional arterioles. We also demonstrated that thrombosis can be induced within the developed arterioles on the chip, suggesting that this device can serve as a viable *in vitro* human arteriole model for studying arterial thrombosis.

Received 29th May 2025,
Accepted 25th June 2025

DOI: 10.1039/d5lc00530b

rsc.li/loc

Open Access Article. Published on 10 Juli 2025. Downloaded on 31.01.26 02:39:04.
This article is licensed under a Creative Commons Attribution 3.0 Unported Licence.

Introduction

The cardiovascular system consists of intricate vessel networks that transport vital nutrients, oxygen, and pharmaceutical drugs to tissues and organs, and it also removes metabolic waste. The arterial and venous vessels are layered tubular structures consisting of endothelial cells (ECs), smooth muscle cells (SMCs), and connective tissues.[1] The capillary bed lies between them and has only one layer of endothelium to facilitate mass transportation between blood and the surrounding tissues. Abnormal vessels lead to cardiovascular diseases, which are the leading cause of death around the world.[2] Thus, replicating the human vascular models *in vitro* is critical for better prognosis and drug development.

Vascularized tissue model systems have significantly advanced in recent years. A comprehensive review can be found in ref. 1, 3 and 4. Reported methods that partially replicate *in vivo* vessel structures include lining endothelial cells on the bottom surface of a rectangular[5,6] or a cylindrical microchannel,[7,8] or on a tubular hydrogel channel.[9,10] A more biomimetic approach is to stimulate neovascularization in a 3D cell construct using vasculogenesis and angiogenesis. Co-culturing endothelial cells with stromal cells induces vasculogenesis, forming a vascular network within the gel scaffold.[11–15] On the other hand, a monolayer of endothelial cells in the side channels promotes angiogenic sprouting and develops into perfusable vessels. These two methods can form a vessel network like an *in vivo* capillary bed.[15,16] However, these networks have only one layer of endothelium, and some may have pericytes to support their structure and functions.[17]

[a] *Institute of Biomedical Electronics and Bioinformatics, National Taiwan University, No. 1, Sec.4, Roosevelt Rd., Taipei, 10617, Taiwan, R.O.C*
[b] *Institute of Applied Mechanics, National Taiwan University, No. 1, Sec.4, Roosevelt Rd., Taipei 10617, Taiwan, R.O.C. E-mail: yhhsu@iam.ntu.edu.tw*
[c] *Graduate School of Advanced Technology, National Taiwan University, No. 1, Sec.4, Roosevelt Rd., Taipei 10617, Taiwan, R.O.C*

† Electronic supplementary information (ESI) available. See DOI: https://doi.org/10.1039/d5lc00530b

This journal is © The Royal Society of Chemistry 2025

Open Access Article. Published on 10 Juli 2025. Downloaded on 31.01.26 02:39:04.
This article is licensed under a Creative Commons Attribution 3.0 Unported Licence.

Thus, they can only mimic capillaries' biophysical and biochemical responses and lack a smooth muscle layer to serve as a model for arterial studies.

In addition to vessel structure, the types of ECs also play an important role in vessel functions and responses. A discussion on EC sourcing can be found in ref. 18. Most studies use human umbilical vein ECs (HUVECs) and human microvascular ECs (HMVECs), which may not have the same gene expression and responses as arterial ECs.[19–21] Therefore, arterial endothelial cells are essential for constructing artery-on-a-chip models to study artery-related diseases and develop targeted therapeutics. In this study, we use human umbilical artery ECs (HUAECs) to retain arterial gene expression and hemodynamic responses.

To date, very limited numbers of studies have reported arterial-like vessels on a chip. The first study inserted a mouse mesenteric arterial segment into a microfluidic device.[22,23] The artery retained its contractility and could be stimulated on the chip. The second study sequentially seeded human aortic smooth muscle cells (HASMCs) and HUVECS in a cylindrical collagen-I channel to create a layered structure.[24] However, muscle contraction is limited due to the thick collagen wall.

On the other hand, only a few reports use primary arterial ECs in organ-on-a-chip devices. For example, Hirth *et al.* created an arteriole–venule microcirculation system using HUAECs and HUVECs for leukocyte trafficking studies.[25] Su *et al.* lined two channels of a quad-channel microfluidic device with primary human aortic ECs (PHAECs) and human aortic SMCs (PHASMCs) that sandwiched a layer of subendothelial extracellular matrix (ECM) between them.[26] This design mimicked an arterial wall and enabled the study of early atherosclerosis. A layered arterial structure can also be emulated using a porous membrane as a substrate, with PHAECs and PHASMCs seeded on opposite sides of the membrane to study vascular diseases, and signalling between the endothelium and SMCs can be studied.[27,28] Nevertheless, these methods are based on the 3-D or 2-D scaffolding to grow an endothelium using arterial ECs. However, they are not self-assembled arterioles that still lack co-localization of the endothelium and the outer smooth muscle layer. Thus, these models cannot respond to hemodynamic signals and regulate vascular tone.

To replicate the *in vivo* layered arterial structure on a chip, we developed a physiological approach to create an arteriole-on-a-chip (AoC) model using human umbilical artery ECs (HUAECs), human umbilical SMCs (HUSMCs), and normal human lung fibroblasts (NHLFs). This method is based on the arteriogenic process found in animal studies, which is induced by a sudden elevated shear stress in a shunt vessel that connects two arteries when one of the arteries is obstructed.[29,30] This mechanism differs from the physiological stimuli of vasculogenesis and angiogenesis, which are based on hypoxia or a high interstitial flow.[31]

The developed physiological approach is the following: a perfusable vascular network was first obtained by sequentially inducing vasculogenesis and angiogenesis processes. Then, arteriogenesis was induced by introducing oscillating shear flow on the endothelium of the vascular network. Our experimental studies demonstrated that a vessel network can be developed into an arterial network where the HUAEC endothelium is wrapped by the HUSMC layer and the basement membrane. Note that the present method applies oscillatory shear stress on the HUAEC vessel wall, whose influence on vessel remodeling and arteriogenesis has yet to be studied. The oscillatory shear stress only applies to the vessels that are perfused. Therefore, it differs from the studies that introduce interstitial[32,33] or intraluminal[34] flow to regulate vascular homeostasis.

To evaluate the extent of arteriogenesis induced by the shear flow, we investigated two different shear flow conditions and compared them with the static (control) condition in the absence of shear flow. Our experimental studies demonstrated that high shear stress enhanced the perfusability of the vascular network by preserving and enhancing the primary vessel while promoting regression of the secondary vessel. Low shear stress induced a low level of remodeling, improving the perfusability of the vascular network, whereas the absence of shear stress led to diminished perfusability. To verify the functionality of this arteriole model, we introduced dopamine to study vasodilation and vasoconstriction across different dosage levels. We further demonstrated that the developed arteriole model was perfusable with human blood and can be used to study arterial thrombosis. These results suggest that the present self-assembled arteriole-on-a-chip model serves as a representative human arterial model, as it has a fully developed layered arterial structure with proper biophysical and biochemical signaling.

Materials and methods

To sequentially introduce vasculogenesis, angiogenesis, and then arteriogenesis in a standard tri-channel microfluidic device to develop an arteriole model, we applied the analogy between the microfluidic channel and the resistive circuit to control the mass transport inside the arteriole chamber and perfused vessels.[35] The following two sections address the design concepts and the microfluidic configurations. The developed protocols are described in the third section.

Create hypoxia to induce vasculogenesis and angiogenesis

Fig. 1A shows the design of the microfluidic configuration to develop a perfused vessel network through vasculogenic and angiogenic processes. The arteriole-on-a-chip (AoC) device is placed at the center, and it has a central arteriole chamber (AC) that is sandwiched by two symmetrically arranged side channels (SCs). The AC and two SCs were connected through 3 pores on each side. The height of the AoC device was 150 μm, the lateral dimension of the AC was 23.21 mm by 0.765 mm, and the width of the SCs was 200 μm. The cell construct was loaded into the AC *via* the

Open Access Article. Published on 10 Juli 2025. Downloaded on 31.01.26 02:39:04.
This article is licensed under a Creative Commons Attribution 3.0 Unported Licence.

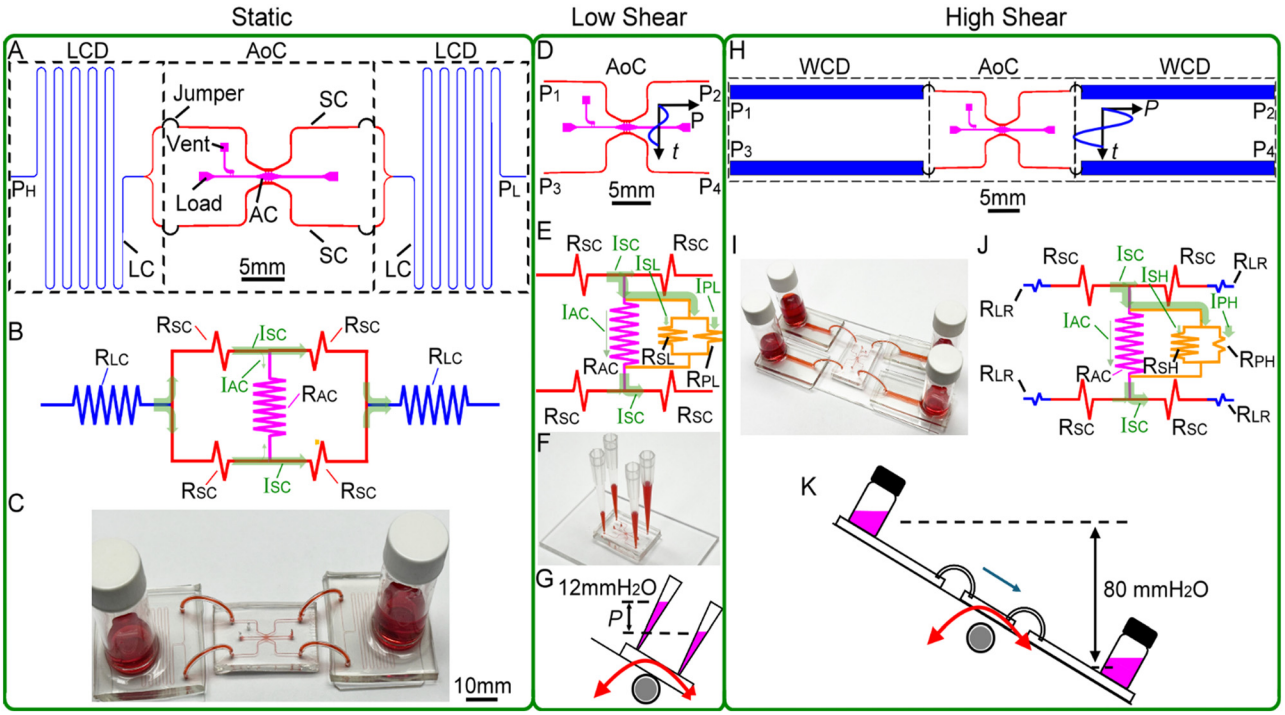

Fig. 1 Microfluidic configurations, equivalent resistive circuits, and setups for inducing static and hypoxic conditions for stimulating vasculogenesis and angiogenesis (A–C), and the low shear stress (D–G) and the high shear stress setups (H–K) for studying arteriogenesis.

load port (load), and a vent channel was designed to release excess pressure to prevent the cell construct from leaking into the two side channels (SCs). The cell construct comprised HUAECs, HUSMCs, and NHLFs suspensions in a bovine fibrin gel.

To create a hypoxic environment, a static condition was created inside the AC by connecting two long-channel devices (LCDs) on two sides of the AoC device. Each long microchannel (LC) was 263.5 mm long with a 100 μm by 100 μm cross-section, and one end was split into two channels and connected to the two side channels (SCs) of the AoC device using equal-length Tygon tubes (jumpers). The other ends were attached with glass vials, and a media height difference (P_H–P_L) of 10 mmH_2O was applied to the two LCDs to drive the media flow. This design created a symmetric pressure drop across the AC, and the connection of two long channels made the pressure drop across the AC to be extremely small. Therefore, a static condition dominated by diffusion was created, and hypoxia can be created inside the arteriole chamber (AC) by placing the device in a 5% O_2 incubator to induce hypoxia, as described in a previously reported method.[11,13]

Fig. 1B shows the equivalent resistive circuit of this microfluidic configuration. The cells and fibrin gel inside the AC created a large hydraulic resistance R_{AC}. It is symmetrically sandwiched between the two short side channels and split channels of the two LC devices, which are simulated as two R_{SC} resistors for each side. This symmetric design makes a very small amount of media (I_{AC}) flow into R_{AC}, and the majority of the media (I_{SC}) flow into the downstream of the R_{SC}, representing the diffusion-dominated mass transport. The resistances of the two long channels are labeled as R_{LC}. The LC devices (LCDs) created a large serial resistance R_{LC} of 5.13×10^{13} Pa s m^{-3}. This design significantly slowed down the flow rate where the reduced media height was less than 10% in 24 hours. The media height was adjusted daily to maintain this static condition. The calculated R_{SC} was 2.96×10^{11} Pa s m^{-3}, which was 3 orders smaller than R_{LC}. Therefore, only a 0.029 cmH_2O pressure drop was applied across the AoC device. Fig. S1A† shows the finite element analysis of the diffusion-dominated arteriole chamber (AC), where a nearly zero pressure gradient was applied. The simulated results (S1B, C and F†) and experimental verification (S1D, E and G†) of the diffusion patterns at 1.75 hours and 3.75 hours demonstrated the effectiveness of this design. Using this microfluidic configuration, vasculogenesis can be induced to grow a HUAEC vessel network inside AC, followed by the angiogenic process to create anastomoses for connecting the side channels with the vessels. Fig. 1C shows the setup of this configuration.

Create an oscillating shear flow to study arteriogenesis

After culturing the AoC device under the static condition for 7 days, a HUAEC vessel network was developed and started to perfuse. We then introduced a low and a high oscillatory pressure to the perfused vessels to study arteriogenesis. During this second phase of the experimental process, the two LCDs were removed to allow for the induction of

This journal is © The Royal Society of Chemistry 2025

Open Access Article. Published on 10 Juli 2025. Downloaded on 31.01.26 02:39:04.
This article is licensed under a Creative Commons Attribution 3.0 Unported Licence.

convective flow, which was applied to the top and bottom side channels using different pressure levels and a rocker.

Fig. 1D and E show the microfluidic configuration and the equivalent circuit to produce a low cyclic pressure and apply a low oscillatory shear stress on the vessel wall. Four pipette tips were gently tugged at the inlets and outlets of the two side channels of the AoC device (Fig. 1F), creating an 11 mm separation. The media height in each pipette tip was initially adjusted to P_1 = 30 mmH_2O, P_2 = 25 mmH_2O, P_3 = 25 mmH_2O, and P_4 = 20 mmH_2O. Following this setup, the device was placed on a rocker to generate a 1 Hz cyclic pressure by tilting between −45° and 45°, as illustrated in Fig. 1G. Due to the hydrostatic pressure driven by the media height difference and rocking of the device, convection dominates mass transport. The majority of media flow in the SC of the top high-pressure side I_{SC} flow into the arteriole chamber (AC). Since the perfused vessels (R_{PL} and R_{SL}) have a much lower resistance than the interstitial space (R_{AC}) created by the NHLFs and HUSMCs, only a small portion of media flow I_{AC} into the interstitial space. The majority of the media will flow into the primary vessel (R_{PL}) and the secondary vessel (R_{SL}). The primary vessel (R_{PL}) represents perfused vessels with larger diameters and lower resistance, which result in a larger media flow (I_{PL}). The secondary vessels (R_{SL}) represent perfused vessels with smaller diameters and higher resistance, which have a smaller media flow I_{SL}. Subscript L stands for the equivalent resistance of vessels under low shear stress conditions. The calculated cyclic pressure to drive the low shear condition was 82.37 Pa across the AC and the vessel network.

To create high cyclic pressure, the two side channels were connected to long and wide microchannel devices (WCDs) on each side of the AoC device, with a glass vial attached to one end to control media height, as shown in Fig. 1H and I. The dimensions of these wide microchannels were 30 mm long by 2 mm wide by 300 μm high. These channels created a very small hydraulic resistance R_{LR} = 5.07E9 Pa s m^{-3} that connected serially to R_{SC}, as shown in Fig. 1J. Thus, 98.3% pressure can be applied on the AoC device. This design extended the distance between glass vials to 90 mm, and the cyclic pressure can be largely increased during the rocking process, as shown in Fig. 1K. The media height of the glass vials was initially adjusted to P_1 = 15 mmH_2O, P_2 = 10 mm H_2O, P_3 = 10 mmH_2O and P_4 = 5 mmH_2O. This setup can simulate a 1 Hz oscillating pressure of 785 Pa (80 mmH_20), which was 9.53 times higher than the low-shear flow setup. This cyclic pressure was applied to the interstitial space and the perfused vessels, where the majority of media also flow into the primary vessel (R_{PH}) and the secondary vessel (R_{SH}), which are represented by I_{PH} and I_{SH}. Subscript H represents the equivalent resistance of vessels under high shear stress conditions.

These two setups allowed us to introduce two different levels of oscillating shear stress on the HUAEC vessel wall. Two factors determined the level of shear stress inside an arteriole. The first factor was the pressure applied at the pores on two sides of the arteriole chamber connected to the side channels. The second factor was the dimensions of the perfused HUAEC vessels. Vessels with larger diameters were classified as primary vessels, while those with smaller diameters were considered secondary vessels. In Fig. 1E and J, R_{PL} and R_{PH} represent the hydraulic resistance of primary vessels. Owing to their larger diameters, primary vessels exhibit reduced hydraulic resistance and thus carry the majority of the flow. In contrast, the smaller secondary vessels, R_{SL} and R_{SH}, have higher resistance and contribute less to the overall flow. Importantly, the hydraulic resistances of both primary and secondary vessels are significantly lower than that of the surrounding tissue (R_{AC}). Consequently, media flowing through the arteriole chip (AC) preferentially travels through the primary vessels. This sustained flow further enlarges the primary vessel, while limited flow through secondary vessels leads to their regression, dynamically optimizing the vascular network.

Physiological approach to develop arteriole-on-a-chip

Fig. 2A to E show the developed physiological approach to grow arterioles on a chip. The ratio of HUAECs, NHLFs, and HUSMCs cell suspension was $0.89 \times 10^7 : 0.89 \times 10^7 : 0.22 \times 10^7$ cells mL^{-1}. They were mixed with a bovine fibrin gel with the final thrombin concentration of 1.1 U mL^{-1} and fibrinogen concentration of 7.89 mg mL^{-1}. This cell construct was first loaded into the central arteriole chamber (AC) (Fig. 2A). The physiological environment of the AC was controlled by the two side channels (SCs), which connected with the AC through three 50 μm wide pores on each side. After fibrin gel solidification in an incubator, endothelial cell media (ScienceCell™, ECM) were filled in the two side channels (SC), and the device was placed in a 5% CO_2/20% O_2/37 °C incubator for 6 hours to allow the cells to settle down. Then, ECM media was replaced with EGM-2 media (LONZA, CC-3162) without VEGF and bFGF (Fig. 2B). The two black arrows show the direction of media flow, which creates a symmetric flow pattern that results in a diffusive-dominated environment as described and shown in Fig. 1A and B. Hypoxia was created in the arteriole chamber by placing the device in a 5% CO_2/5% O_2/37 °C incubator.[13] This hypoxic environment induced vasculogenesis, leading to the formation of a vessel network (Fig. 2B). On day 4, a monolayer of HUAECs (5×10^6 cells per mL) was lined on the exposed fibrin gel at pores to form endothelium (Fig. 2C), followed by flowing HUAEC media into the two side channels. By day 7, the lined endothelium had anastomosed with the preformed network within the chamber through angiogenesis to form a perfusable vascular network (Fig. 2D). The connection and perfusion of the vessels were verified using FITC-labeled 70 kDa dextran on day 7. Once the vessels were perfused, a static, low-level, or high-level oscillating shear flow was applied to introduce oscillatory shear stress in the perfused vessel tree (Fig. 2E). The oscillating shear flow was indicated with double-headed arrows. The static

Open Access Article. Published on 10 Juli 2025. Downloaded on 31.01.26 02:39:04.
This article is licensed under a Creative Commons Attribution 3.0 Unported Licence.

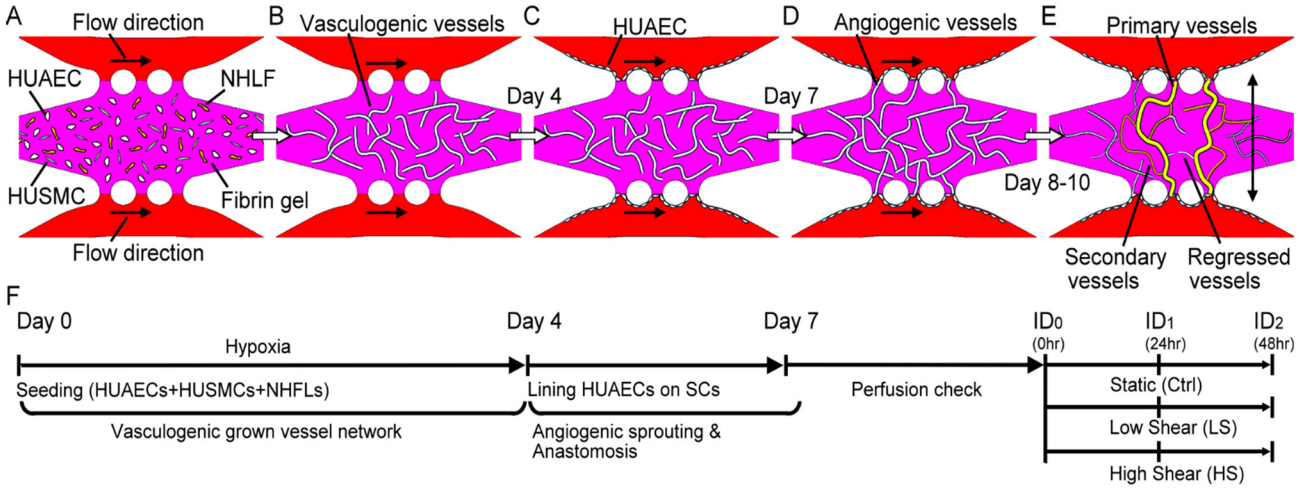

Fig. 2 Illustrations of the experimental protocol for developing an arteriole model in the AoC device (A–F). On day 0, HUAECs, NHLF and HUSMCs were seeded and co-cultured in the arteriole chamber (A). Vasculogenic vessels developed by day 4 (B) and HUAEC monolayer was seeded on the side channels (C). By day 7, angiogenic vessels grew from the side channels and anastomosed with the existing vasculogenic vessels (D). Once the vessels started to perfuse, a static, low shear stress, or high shear stress physiological environment was induced in the perfused vessels from inspection day 0 (ID_0) to inspection day 1 (ID_1) and day 2 (ID_2) (E). The experimental timeline of the developed protocol (F). Black arrows represent the direction of media flow. The double-headed arrow represents the oscillatory flow under two different cyclic pressures.

condition was to culture the AoC device under the diffusion-dominated setup shown in Fig. 1A. Fig. 1F summarizes the developed protocols. On the day we started to study the remodeling of the HUAEC vessels, we designated it as the inspection day 0 (ID_0), and the remodeling process of the vessels was investigated for two days to study the induction of arteriogenesis by identifying the primary, secondary, and regressing vessels. The vessels were inspected during the 24th hour and the 48th hour and labeled as ID_1 and ID_2.

Study vessel remodeling under oscillating shear flow

To verify that the applied shear stress could mediate HUAEC vessel remodeling, the devices were subjected to low and high shear stress conditions using a rocker platform for two days, as shown in Fig. 1D–G and H–K. Both shear stress conditions were compared to the static condition. As described above, the static culture conditions were maintained for the control devices without any applied flow (Fig. 1A–C). The vessel remodeling process was monitored by perfusing 70 kDa FITC-labeled dextran every 24 hours after applying shear stress. Vascular parameters such as diameters, branch points, segment length, and number of branch segments were compared to understand the effect of shear stress on arteriole development. After rocking for 48 hours, the devices were fixed, and vessel structures were investigated. The nuclei, endothelium, SMC layer, and basement membrane (BM) were stained with H33342 (Invitrogen), PE-conjugated CD31 antibody (Invitrogen), FITC-conjugated calponin antibody (Fabgennix), and Alexa Fluor™ 647-labeled collagen IV antibody (Invitrogen), respectively. The collagen IV images revealed the basement membrane (BM) structure, representing the initial vascular network formed through vasculogenesis, and the CD31 represented the final vessel structure after applying 48 hours of oscillating shear stress. The diameters and areas of the BM and vessel network were measured to quantify the extent of the vessel remodeling process.

Assays to verify arteriole functionality

Two experiments were conducted to verify the functionality of the developed arterioles. First, their ability to undergo vasoconstriction and vasodilation was assessed using dopamine stimulation. Studies have shown that low dopamine dosage (0.5 to 2 mg kg^{-1} per minute) acts as a vasodilator, whereas higher dosage (>10 mg kg^{-1} per minute) acts as a vasoconstrictor.[36] Mixed behavior was found in the medium dosage. For our studies, we used matured arterioles developed until day 10. The long and wide channel devices (WCDs) were replaced with pipette tips, and different concentrations of dopamine mixed with the FITC-labeled dextran in a PBS solution were introduced at one end of the side channels with a 15 mmH_2O driving pressure. This allowed the dopamine to flow through the arterioles, and the vasoconstriction and vasodilation processes were monitored using a fluorescent inverted microscope (OLYMPUS IX71). After each dopamine dosage, the arterioles were flushed with PBS, and sufficient time was allowed for them to return to their original structure before proceeding with the next experiment. Changes in vessel diameters were quantified to assess whether the arterioles underwent constriction or dilation.

The second validation experiment aimed to assess the ability to induce arterial thrombosis. We investigated whether the secretion of von Willebrand factor (vWF) from the

 This journal is © The Royal Society of Chemistry 2025

Open Access Article. Published on 10 Juli 2025. Downloaded on 31.01.26 02:39:04.
This article is licensed under a Creative Commons Attribution 3.0 Unported Licence.

endothelial cells could trigger thrombosis. The vWF is a glycoprotein released by injured endothelial cells that facilitates platelet adhesion and blood clot formation to seal the vascular injury.[37] It is primarily involved in thrombogenesis, and an abnormal deficiency of vWF-cleaving metalloprotease (such as ADAMTS13) can lead to an increased risk of arterial thrombosis. Phorbol 12-myristate 13-acetate (PMA), a phorbol ester, was used to stimulate endothelial release of vWF, and blood clot formation was assessed by staining for platelets.[38,39] The experimental summary is as follows. Matured arterioles on day 10 were used for this study. Initially, human blood was perfused through the arterioles to confirm that the developed vessels did not spontaneously induce thrombosis. To stimulate von Willebrand factor (vWF) release from endothelial cells, the devices were then perfused with 50 ng mL^{-1} Phorbol 12-myristate 13-acetate (PMA; Sigma-Aldrich) diluted in ECM media and incubated for 30 minutes. Following incubation, the arterioles were flushed with PBS and subsequently perfused with human blood to investigate the induction of arterial thrombosis. After perfusion, the blood was flushed out using PBS, and the arterioles were fixed for analysis.

To verify vWF release from the endothelium, the arterioles were stained with FITC-conjugated anti-vWF antibody (Abcam). Platelet adhesion and clot formation were visualized by staining with PE-labeled anti-CD41a antibody (Invitrogen), which allowed identification of thrombosis sites.

Whole blood acquisition

Fresh human blood was drawn into a blood collection tube with 3.8% sodium citrate from a healthy donor who consented to participate in this study. Fresh blood was introduced to the AoC within 2 hours to study arteriole thrombosis. All experiments were performed in accordance with the Guidelines of Human Subjects Research Act, and experiments were approved by the ethics committee at National Taiwan University (202112MH021). Informed consents were obtained from human participants of this study.

Cell culture

HUAECs and HASMCs were purchased from ScienCell™ and cultured in endothelial culture medium (ECM), and smooth muscle cell medium (SMCM) was purchased from the vendor. NHLFs were purchased from Lonza and were cultured in Fibroblast Growth Medium-2 BulletKit™ (FGM™-2). The cells were cultured in a 5% CO_2 and 37 °C incubator. Fresh culture media were replaced every two days, and cells were maintained until they reached approximately 90% confluency before being passaged for experiments.

Immunohistochemistry protocol

The devices were fixed using 4% paraformaldehyde solution for 30 minutes and then washed with 0.1% Triton thrice every 10 minutes. Next, the devices were permeabilized with 0.5% Triton for 30 minutes before blocking with 3% BSA. Devices were immuostained for 3–4 days at 4 °C. All devices were washed with PBS thrice before fluorescent imaging.

Quantification and analysis

The dynamic remodeling process of the HUAEC vessels was monitored every 24 hours by flowing the FITC-labeled dextran solution and recorded using an inverted fluorescent microscope (Olympus X71). The immunostained AoC devices were imaged using a spin-disk confocal microscope (Andor-BC43, Oxford Instruments). Then, these images were analyzed using the ImageJ software. The vessel parameters were quantified, such as diameter, area, number of branches and nodes, SMC and collagen-IV areas. Parametric or non-parametric tests were performed after checking for the normality of the data distribution and homogeneity of variances using GraphPad Prism software. Statistical significance was determined as $p < 0.05$. Each experiment was repeated at least three times.

Fabrication

The fabrication process is the same as our previously published paper.[11] Briefly, a SU-8 master was first constructed on Piranha cleaned 4″ silicon wafers, followed by the standard photolithography process. A SU-82050 photoresist was used to create 150 μm and 100 μm height masters for making AoC and LC devices. After the SU-8 master was hard-baked, PDMS prepolymer and curing agent in a 10-to-1 ratio were mixed and poured on the SU-8 masters to conduct micro-molding. Once the PDMS was cured, the molded microchannels were demolded, punched holes, and then bonded to another PDMS spin-coated cover glass using O_2 plasma. Then, the AoC and LC devices were placed on a 1 mm-thick PMMA to assemble the device with Tygon tubes. The PDMS devices were sterilized using an autoclave, and the PMMA sheets were sterilized using UVC light.

Finite element analysis

COMSOL Multiphysics® was used to study the induced physiological environment in the culture chamber. A 3-D model of the AoC device was constructed, which was connected with two long-channel devices (LCDs). Hydrostatic pressures of P_H = 98 Pa and P_L = 0 Pa were applied at the entrance and exit of the two LCDs, while non-slip boundary conditions were applied to all other surfaces. The resultant mass transport inside the culture chamber was studied using the steady state analysis, followed by a time-dependent analysis of the nutrition delivery from the long microchannels.

The three-dimensional geometry of the primary and secondary arterioles was reconstructed from the IMARIS software using one of the developed arteriole 3-D images. The 3-D image was imported into a finite element software (COMSOL Multiphysics®) for simulation. The velocity

Open Access Article. Published on 10 Juli 2025. Downloaded on 31.01.26 02:39:04.
This article is licensed under a Creative Commons Attribution 3.0 Unported Licence.

profile and wall shear stress of the basement membrane (BM) and the vessel network (Endo) of the primary and secondary vessels were simulated to study the initial and final vessel structure after applying the high shear stress condition. To simulate high-flow conditions and the resulting shear stress, the inlet of the arteriole was set to 785 Pa, while the outlet was set to 0 Pa. Non-slip boundary conditions were set to the inner surface of the arterioles. Then, a steady-state analysis was conducted to study the hydrodynamic environment, including velocity profiles and shear stress. The parameters used for the finite element analysis are summarized in the following: media density and dynamic viscosity were 0.99 kg m^{-3} and 0.7 mPa; the porosity and permeability of the fibrin gel were 0.99 and 1.5×10^{-13} m^2; the concentration of nutrition was 1 mol m^{-3} with a diffusion coefficient of 7×10^{-11} m^2 s^{-1}; the temperature was 310.15 K.

Results

Influence of the oscillating shear stress on the arteriole network structure

Fig. 3A–C show the representative vessel structures developed under static (Ctrl), low oscillating shear stress (LS), and high oscillating shear stress (HS) conditions. The endothelium, SMC layer, and the BM were visualized using IMARIS software and represented with red, green, and magenta pseudo-colors, respectively. To better visualize the HUAEC vessels and SMCs, the IMARIS Surface module was used to reconstruct the vessel structures, which are shown in Fig. 3D–F, respectively. Quantified measurements of vessel diameter, vessel area (CD 31), SMC area (Calponin), and BM (Col IV) area are summarized in Fig. 3G–J, respectively. The vessels formed in the HS condition were found to have larger, longer, and more intricate structures than the other two conditions. The measured median vessel diameter of the HS condition was 28 ± 10.8 μm, which was significantly larger than the LS (14 ± 5.53 μm) and Ctrl (16 ± 8.05 μm) conditions (Fig. 3G). Furthermore, the average vessel area of the HS conditions was also significantly larger than the other two conditions, measuring 46.7% ± 8.4%, compared to 20.6% ± 4.1% under LS conditions and 13.7% ± 2.6% under static conditions (Fig. 3H). Notably, the total vessel area was lowest under static conditions. The vessel diameter in the static condition was relatively larger than in the LS condition and remained significantly smaller than in the HS condition (Fig. 3G). When compared to the perfused and connected vessels analyzed in the subsequent section, only a limited number of vessels appeared to be connected and perfused under the static condition (Fig. 4A). In comparison, a greater number of vessels were connected under LS and HS conditions (Fig. 4B and C). These results suggest that HUAEC vessels developed under static conditions were sparsely connected and exhibited limited perfusability through both inter-vessel connections and pores of the AoC device. In contrast, vessels exposed to low shear (LS) conditions developed longer structures with smaller diameters but showed enhanced perfusability, likely due to increased connectivity within the vascular network. The vessel structure became

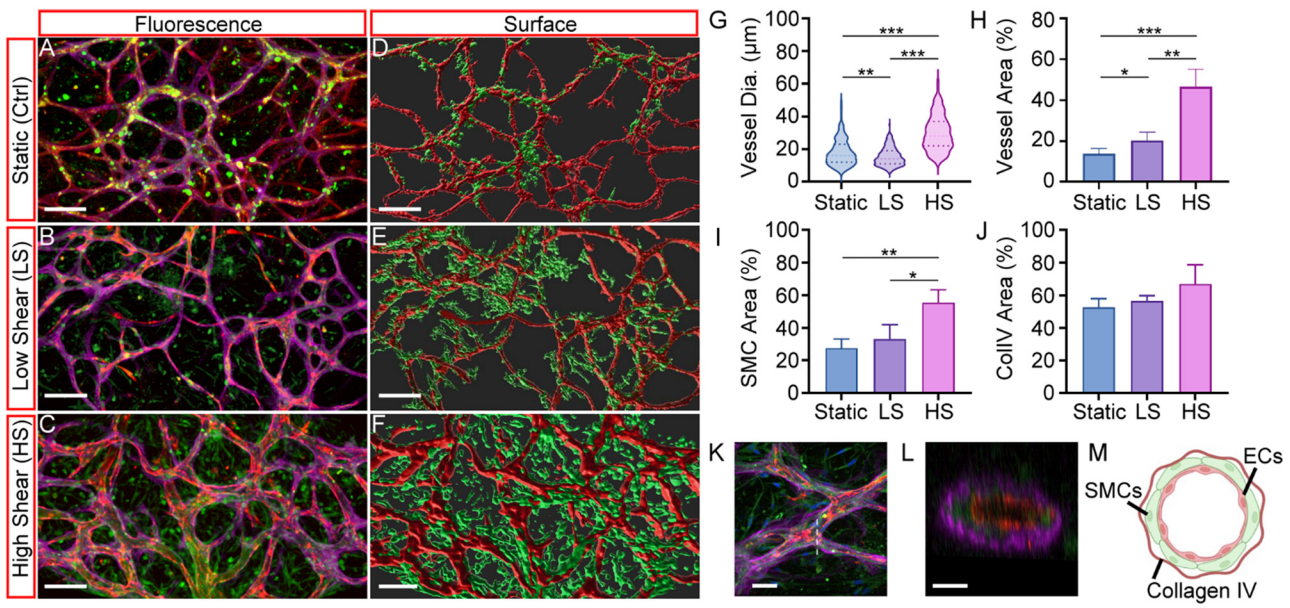

Fig. 3 Fluorescent micrographs and IMARIS Surface images of the vessels developed under static (Ctrl) (A and D), low (LS) (B and E), and high (HS) (C and F) oscillating shear stress. Statistical analysis of vessel diameter (G), vessel area (H), SMC area (I), and CollV area (J). Each condition was repeated 3 to 4 times, and the total number of measured vessels was 68, 115, and 112 for the static, LS, and HS conditions. Fluorescent micrographs (K) and cross-sectional micrographs of an arteriole section developed under HS conditions (L), and an illustration of the self-assembled arteriole structure (M) (image partially done with **http://Biorender.com**). HUAEC vessels, SMC layer, and basement membrane are stained with endothelium (red), SMC (green), and BM (magenta) (scale bar = 150 μm (A–F), 40 μm (K), 10 μm (L)).

This journal is © The Royal Society of Chemistry 2025

Open Access Article. Published on 10 Juli 2025. Downloaded on 31.01.26 02:39:04.
This article is licensed under a Creative Commons Attribution 3.0 Unported Licence.

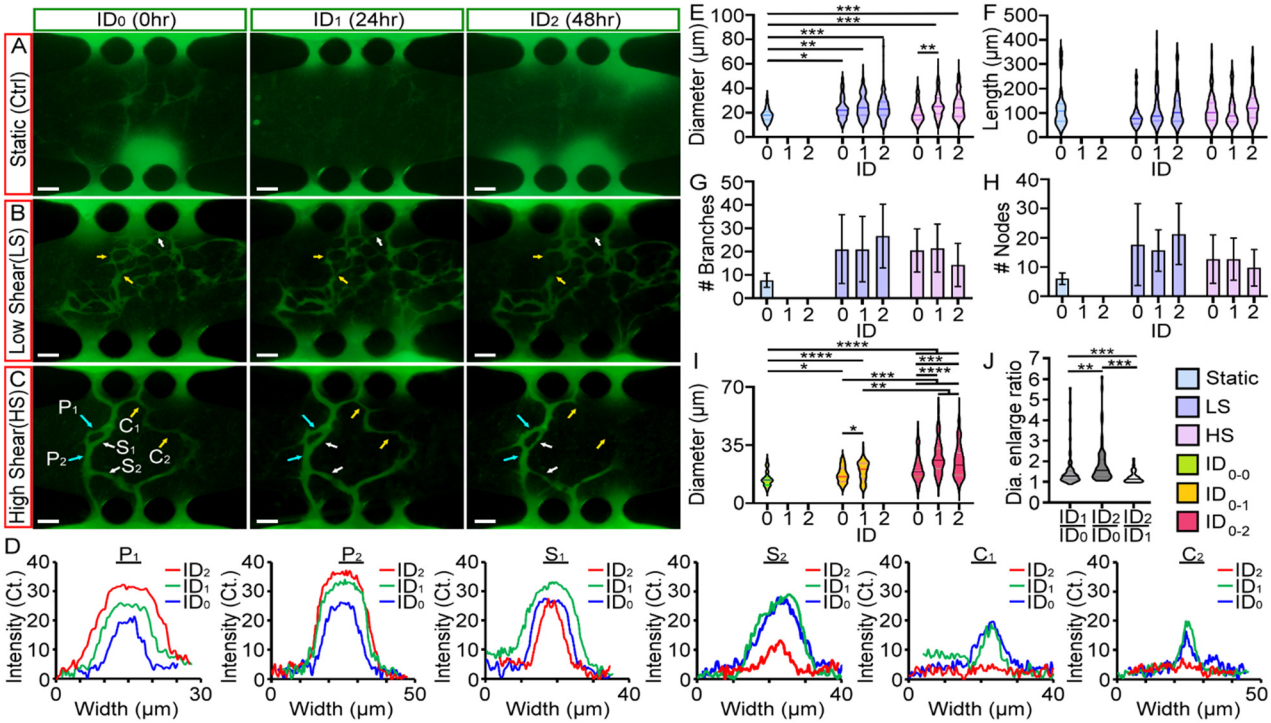

Fig. 4 Fluorescent micrographs of the HUAEC vessels grown under static (Ctrl) (A), low (LS) (B), and High (HS) (C) oscillating shear stress over 48 hours. Intensity profiles of the cross-sections of the P_1, P_2, S_1, S_2, C_1, and C_2 labelled vessels cultured under the HS condition (D). Statistical analysis of the vessel diameter (E), length (F), number of branches (G), and nodes (H). Each condition was repeated 3 to 4 times, and the total number of measured vessels was 18, 50, and 37 for the static, LS, and HS conditions. Comparisons of diameters of vessels that only perfused on ID_0 (day_{0-0}), perfused from ID_0 to ID_1 (day_{0-1}) and from ID0 to ID_2 (day_{0-2}) (I), and the diameter enlarge ratio between ID_1 to ID_0 (ID_1/ID_0), ID_2 to ID_0 (ID_2/ID_0), and ID_2 to ID_1 (ID_2/ID_1) (J) (scale bar = 100 μm).

much larger when a higher shear stress was applied using the HS condition.

These results demonstrate a direct correlation between enhanced arteriolar network and the level of oscillating shear stress. Elevated shear stress promotes vessel structural integrity and maturation, whereas static conditions impede vessel formation and slow down the network development. Similar results were also found for the SMC area. The measured SMC area under HS conditions was 55.4% ± 7.9% (Fig. 2I), which was significantly greater than that of the LS conditions (33.1% ± 8.8%) and static conditions (27.5% ± 5.5%). The BM area was comparable across all three conditions, with only a slight and statistically insignificant increase observed under HS conditions.

Finally, we investigated the HUAEC vessel structure developed under the HS condition. Fig. 3K highlights the region (indicated by the white dashed line) selected from one of the arteriole devices, and the corresponding cross-sectional view of this section is shown in Fig. 3L. It shows that the arteriole-like vessel structure (Fig. 3M) was successfully self-assembled. The vessel lumen exhibited a concentric organization, consisting of an inner layer of HUAEC endothelium (red), surrounded by smooth muscle cells (green), and enclosed by an outer BM layer (magenta).

Effect of oscillating shear stress in dynamic HUAEC vessel remodeling

To visualize the dynamic remodeling of the HUAEC vessels, FITC-labeled dextran was flown into the vessels every 24 hours from day 7 to day 10. Fig. 4A–C show the fluorescent micrographs of the vessels grown under static (Ctrl), low (LS), and high (HS) oscillating shear stress conditions. The onset, the 24th hour, and the 48th hour of introducing cyclic shear stress into the vessels are labeled as ID_0 (0 h), ID_1 (24 h), and ID_2 (48 h).

For static condition (Fig. 4A), it was found that the perfused HUAEC vessel network gradually reduced over 48 hours, and many of the vessels lost connection by day 9. In contrast, under the LS condition, vessel perfusability increased progressively over time, accompanied by enhanced completeness of network connectivity (Fig. 4B). However, after 48 hours of culture under LS conditions, some vessels became thinner or disconnected, as labeled with white and yellow arrows, respectively. In contrast, at increased oscillating flow, a distinct vascular remodeling process was observed for the HS condition, as shown in Fig. 4C. It was observed that larger vessels expanded (light blue arrows, P_1 and P_2), while smaller vessels thinned (white arrows, S_1 and S_2) or ceased to perfuse (yellow arrows, C_1 and C_2), indicating regression of these secondary vessels. Fig. 4D shows the

Open Access Article. Published on 10 Juli 2025. Downloaded on 31.01.26 02:39:04.
This article is licensed under a Creative Commons Attribution 3.0 Unported Licence.

intensity profiles of the cross-sections of the labeled vessels over the 48 hour application of the HS condition, where blue, green, and red lines represent the vessel diameters measured on ID_0, ID_1, and ID_2, respectively. The increased fluorescent intensity and width of the primary vessels P_1 and P_2 suggest that these vessels were enlarged. On the other hand, the reduction of fluorescent intensity and width of the secondary vessels S_1 and S_2 from ID_1 to ID_2 demonstrates the thinning process of the smaller vessels. The C_1 and C_2 vessels that became disconnected were also from ID_1 to ID_2. These findings are pivotal for understanding HUAEC vessel remodeling, wherein a specific level of shear stress leads to the regression of secondary vessels, while primary vessels remain perfused and structurally reinforced. This result suggests that the developed arterioles can effectively respond to wall shear stress and undergo structural reconstruction, ultimately evolving into a more efficient arteriolar network.

To quantify the vessel remodeling process, we measured dynamic changes in vessel diameter (Fig. 4E), vessel length (Fig. 4F), as well as the number of branches (Fig. 4G) and junctions (Fig. 4H). It was found that the median diameter of the static condition was 18 ± 5.3 μm on ID_0, and no observable vessels were detected for the remainder of the experiment. The range and distributions of the vessel length did not have significant differences compared to the other two conditions.

For the LS condition, the measured median vessel diameter was 22 ± 9.1 μm, 24 ± 9.5 μm, and 23 ± 10.3 μm for ID_0, ID_1, and ID_2, respectively (Fig. 4E). Although there was a slight increment in diameter over the 48 hour period, the difference was insignificant. Similarly, the vessel length and the number of branches and nodes were either maintained or increased slightly over the 48-hour period in the LS condition. These findings underscore the critical role of low shear stress in promoting the development and stabilization of luminal structures, thereby ensuring sustained vessel perfusion.

In contrast, the median vessel diameter under the HS condition showed a significant increase from ID_0 to ID_1, rising from 18 ± 7.9 μm to 25 ± 9.6 μm, and remained relatively stable at 24 ± 10.03 μm on ID_2. Furthermore, the number of branches and nodes under the HS condition was relatively lower on ID_2, as shown in Fig. 4G and H. Also, we observed that while some vessels underwent enlargement, others became thinner or regressed, indicated by the white and yellow arrows in Fig. 4C. These observations suggest that applying a high oscillating shear stress on the HUAEC vessel walls can stimulate an extensive arteriogenic process in the first 24 hours. This process can slow down once the vessel diameter enlarges, resulting in a reduction of the wall shear stress.

In summary, our experimental studies show that shear stress levels may play a key role in arteriolar remodeling: low shear stress may promote increased perfusability by encouraging the expansion of the vascular network, whereas high shear stress may optimize the network by stabilizing primary vessels and inducing regression of secondary vessels.

Given that vessel diameter affects intraluminal shear stress, we examined whether the initial diameter of perfused vessels influenced the final state of remodelled vessels. We categorized vessels developed by high oscillating shear stress into three groups: (i) vessels that were perfused only on ID_0 and lost perfusion by ID_1 and ID_2 (Day_{0-0}), (ii) vessels that remained perfused on ID_1 but not on ID_2 (day_{0-1}), and (iii) vessels that remained perfused from ID_0 through ID_2 (day_{0-2}). The vessel diameter for ID_1 and ID_2 in each group was also quantified. The results are summarized in Fig. 4I. The initial median diameter of the day_{0-0} was 14.8 ± 4.5 μm, and it was significantly smaller than the initial median diameters of the day_{0-1} and day_{0-2} vessel groups, which were 17.2 ± 4.9 μm and 21.0 ± 7.9 μm. Also, there was no significant difference between the initial median diameter of the day_{0-1} and day_{0-2} cases.

On the other hand, the median diameter on ID_1 of the day_{0-1} condition was significantly smaller than that of ID_1 of the day_{0-2} condition. These results suggest that the initial diameter of the HUAEC vessels is directly related to the sustenance of the perfusability of the vessels when subjected to high oscillating pressures and the resultant shear stress. Larger vessels tend to grow when introduced to a high-level oscillating shear flow. It suggests that HUAEC vessels with a larger diameter can be stimulated to enlarge and develop into a functional arteriole.

Next, we investigated the daily changes in diameter for vessels that remained perfused from ID_0 through ID_2 (day_{0-2} group), to evaluate how these vessels enlarged over time. We grouped the vessels that continued to grow until ID_2, and quantified their diameter changes over time by calculating the following ratios: ID_1 to ID_0 (ID_1/ID_0), ID_2 to ID_0 (ID_2/ID_0), and ID_2 to ID_1 (ID_2/ID_1). The quantified results are summarized in Fig. 4J. We found that the average diameter enlargement ratios for D_1/D_0 and D_2/D_0 were 1.51 ± 0.83 and 1.83 ± 0.96, respectively. The vessel diameters clearly increased on both ID_1 and ID_2 compared to ID_0, with some vessels exhibiting enlargement by as much as 5.57-fold and 6.14-fold after 1 and 2 days of incubation under high shear conditions, respectively. Interestingly, the diameter enlargement ratio D_2/D_1 was significantly smaller than the D_1/D_0 and D_2/D_0 ratios. The average ratio was reduced to 1.23 ± 0.28 times, and the largest ratio was only up to 2.14. This observation suggests that the sudden application of high shear stress leads to a substantial increase in intraluminal shear, resulting in pronounced vessel dilation within the first 24 hours. However, after the vessel diameter enlargement, the wall shear stress level also reduced, which could be below the physiological range that can stimulate the arterial enlargement. This could also be a function of the arteries, in which the arterial vessels can adapt to the wall shear stress to remodel into a vessel structure with a more stable hemodynamic state. These findings indicate that high shear stress is critical in initiating vessel enlargement and driving structural stabilization of the vascular network.

 This journal is © The Royal Society of Chemistry 2025

Open Access Article. Published on 10 Juli 2025. Downloaded on 31.01.26 02:39:04.
This article is licensed under a Creative Commons Attribution 3.0 Unported Licence.

Investigating HUAEC vessel remodeling using CD31 and collagen IV

From previous results, we observed that shear stress is important in developing arteriole vessels and maintaining their luminal structure for perfusion. *In vivo* studies have shown that basement membranes (BMs) of regressing blood vessels can persist even after the endothelium has regressed.[40] Since our initial vessel network was formed through vasculogenesis, and vessel remodeling was observed during arteriogenesis, the study of the BM and the final vessel structures can effectively visualize the extent of vascular remodeling induced by the three physiological conditions. Hence, we immunostained fixed devices with anti-CD31 and anti-collagen IV to visualize endothelium and basement membrane structures. Collagen IV staining served as a marker for the initial vessel architecture, while CD31 staining represented the induced vessel remodeling after culturing under static, LS, or HS conditions, representing the final endothelial configuration. Fig. 5A and B, D and E, and G and H, present fluorescent micrographs of CD31-labeled HUAEC endothelium (red) and collagen IV-labeled basement membranes (magenta) under static, LS, or HS conditions, respectively. To visualize their spatial correlation, we used the IMARIS Surface module to generate merged 3D renderings of both markers, shown in Fig. 5C, F and I.

As expected, the endothelium and basement membranes (BMs) were co-localized across all three conditions, with a few exceptions. Some BMs lacked associated vessels (indicated by white arrows), while others contained regressing vessels (yellow arrows). Additionally, certain vessels appeared significantly thinner than the surrounding BM layer, suggesting they were undergoing thinning or regression. The presence of BMs without endothelium further supports that these sites correspond to regressed blood vessels. Collectively, these findings recapitulate key features of vascular remodeling observed *in vivo*. Our results confirm that the basement membrane represents the initial vascular network, which undergoes extensive remodeling upon application of shear stress to form an optimized vascular structure.

To quantify the effect of shear stress in remodeling, we measured the diameter and area of the endothelium (CD31) and BMs (ColIV). The results are summarized in Fig. 5J and K. It was found that the diameter of the BMs was generally larger than that of the endothelium, as shown in Fig. 5J. The median diameters of the vessels developed under static, LS, and HS conditions were 16 ± 8.0 μm, 13 ± 5.9 μm, and 27 ± 10.8 μm. The corresponding media BM diameters were 23 ± 10 μm, 20 ± 6.5 μm, and 32 ± 11.9 μm. These differences were partially attributed to the remodeling process of HUAEC vessels and the SMC layers that wrapped around the endothelium to form the arteriole structure. Notably, consistent with our observations of dynamic remodeling, larger-diameter vessels were observed under the high shear (HS) condition, suggesting that high oscillatory shear stress promotes the development of enlarged HUAEC vessels.

On the other hand, there is a significant difference between the endothelium and BM areas for the static (Ctrl) and LS conditions, but not for the HS condition. The BM areas of the static and LS conditions were 52.69 ± 5.29% and

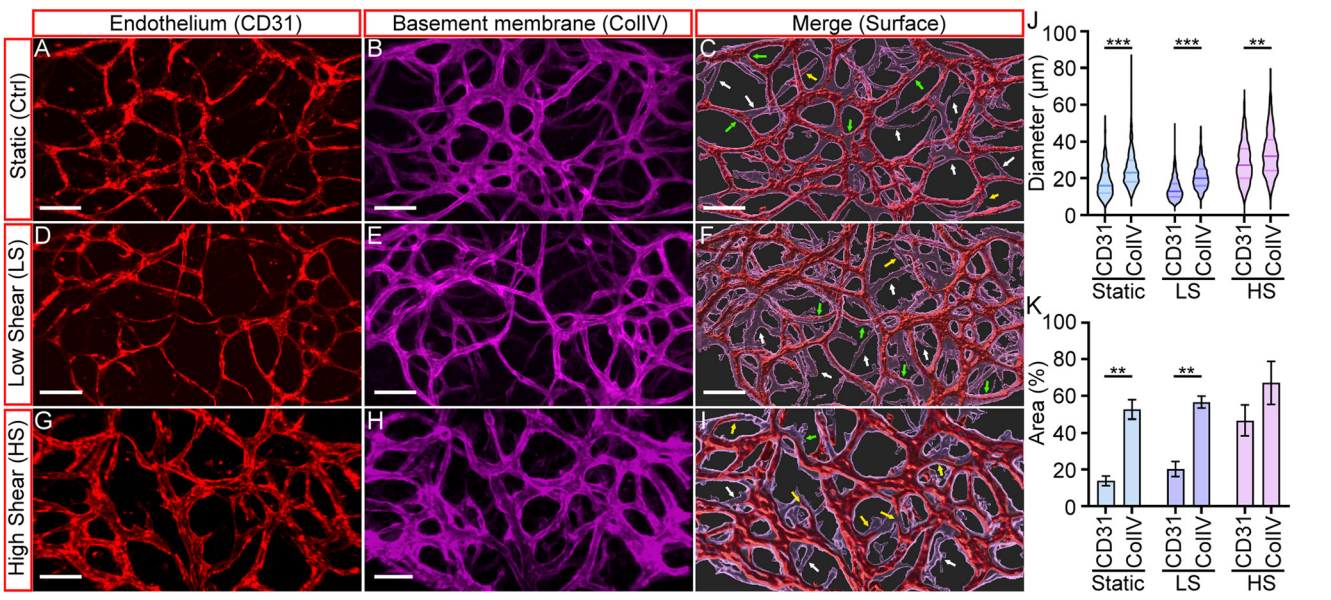

Fig. 5 Fluorescent micrographs of the CD-31 labeled HUAEC endothelium and collagen-IV labeled basement membranes (BMs) under static (Ctrl) (A–C), LS (D–F), and HS (G–I) conditions (n = 3). Statistical analysis of the endothelial and BM diameters (J) and area coverage (K). Each condition was repeated for 3 to 4 times (scale bar = 150 μm).

Open Access Article. Published on 10 Juli 2025. Downloaded on 31.01.26 02:39:04.
This article is licensed under a Creative Commons Attribution 3.0 Unported Licence.

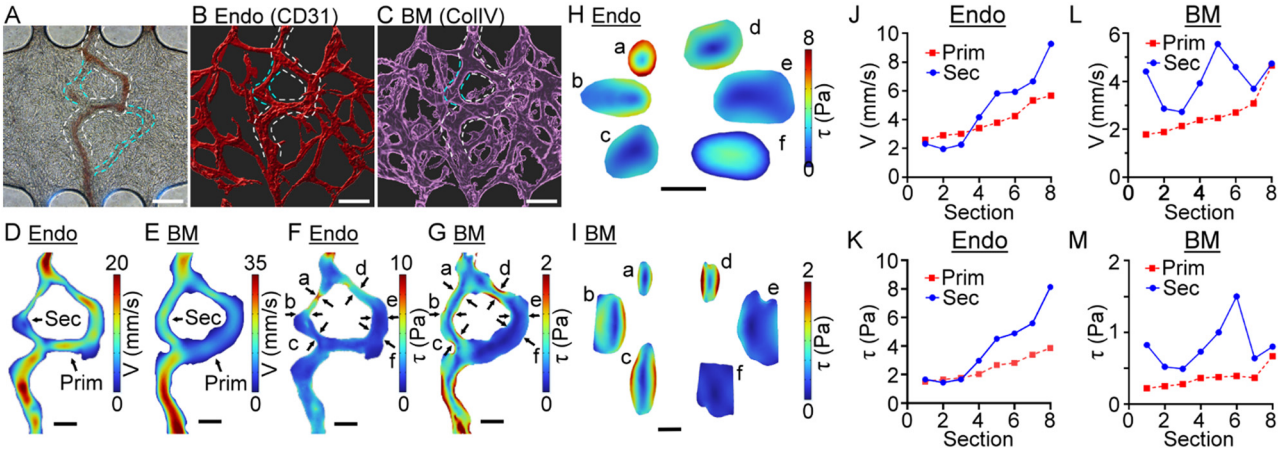

Fig. 6 Finite element analysis of vessel and collagen structures developed under the high oscillating shear stress (HS) condition: micrographs of human blood flowing through a mature artery (A). 3D renderings of the vessel structure (B), and collagen structure (C). Simulated velocity and shear stress profile of fluid flow through representative sections of the primary (Prim) and secondary (Sec) vessel structures (D and F) and collagen structures (E and G). Shear stress at different representative cross-sections of vessel structure (H) and collagen structure (I). Analysed values of fluid velocity and wall shear stress through different cross-sections of the vessel structures (J and K) and collagen structures (L and M). Scale bar = 100 μm (A–C), 50 μm (D–I).

56.62 ± 2.81%, and the endothelium area was 13.57 ± 2.59% and 20.27 ± 3.56%, respectively. In contrast, the endothelium and BM areas of the HS conditions were 46.69 ± 6.87% and 67.05 ± 9.61%, respectively.

Study on arteriole remodeling using finite element analysis

In the preceding sections, we demonstrated that high oscillating shear stress plays a pivotal role in remodeling and maintaining the HUAEC vascular network. We also demonstrated that HUAEC vessels exhibited an arteriole-like structure, characterized by an endothelial layer encased by both a SMC layer and a surrounding basement membrane. Fig. 6A and Video S1† show an image and a video of human blood perfused through an arteriole network that developed after 48 hours of high oscillatory shear stress. This AoC device corresponds to the vessels shown in Fig. 3C, F and G–I. A prominent primary arteriole spanning the chamber and two secondary vessels branching toward the top and bottom regions were observed and are outlined with white and light-blue dashed lines, respectively. Fig. 6B and C display 3D IMARIS surface renderings of CD31-labeled HUAEC endothelium and collagen IV-labeled basement membranes (BMs), respectively.

To assess the wall shear stress and velocity profile within these segments under high shear (HS) conditions, we isolated the IMARIS surface models of the perfused regions and their corresponding BM networks. They are highlighted by dashed lines in Fig. 6B and C using IMARIS Slicer software. These geometries were then imported into COMSOL Multiphysics for the finite element simulation. The segments were modelled under a high-shear hemodynamic environment to evaluate the flow dynamics within the luminal spaces of both the endothelial and BM structures.

Fig. 6D and E show the simulated velocity profiles, and Fig. 6F and G show the corresponding shear stress profiles in the endothelial (Endo) and basement membrane (BM) segments, respectively. The primary and secondary vessels were labeled as Prim and Sec in Fig. 6D and E, respectively.

The tubular structure of the BM layer was generally larger than that enclosed by the endothelium. It was because SMC layers were sandwiched between the endothelium and the BM layer. Nevertheless, it likely represents the original vessel structure before applying high oscillatory shear stress (τ). For both networks, the sampled primary vessel is the *d*, *e*, and *f* cross-sections, and the sampled secondary vessel is from the *a*, *b*, and *c* cross-sections, as shown in Fig. 6F and G. Simulation results of the basement membrane (BM) layers revealed that the secondary network exhibited higher velocity and wall shear stress compared to the primary arteriole, except at position *d*. At this location (*d*), the primary vessel had a narrower lumen, resulting in elevated local wall shear stress. Comparisons of wall shear stress profiles within the Endo and BM structures are presented in Fig. 6H and I. These data indicate that the secondary vessel experienced progressive thinning at positions *a*, *b*, and *c*, corresponding with regions of higher wall shear stress (Fig. 6I). In contrast, the primary vessel showed localized thinning only at position *d* (Fig. 6H).

To quantify the shear stress and velocity within vascular structures, the primary and secondary vessels were segmented into eight sections. For the secondary vessel, measurements were conducted along the path from *c* to *a*, and for the primary vessel, the path was from *f* to *d*. The average velocity and average wall shear stress for the endothelial vessel are shown in Fig. 6J and K. The average

 This journal is © The Royal Society of Chemistry 2025

Open Access Article. Published on 10 Juli 2025. Downloaded on 31.01.26 02:39:04.
This article is licensed under a Creative Commons Attribution 3.0 Unported Licence.

velocity of the primary and the secondary vessels ranged from 2.95 mm s^{-1} to 5.68 mm s^{-1} and from 1.95 mm s^{-1} to 9.35 mm s^{-1}, respectively. Their corresponding average wall shear stress ranged from 1.49 Pa to 3.84 Pa and from 1.42 Pa to 8.13 Pa. It clearly shows that the section that underwent the most thinning process of the secondary vessel, from point 4 to point 8, had a higher average velocity and wall shear stress.

The velocity and shear stress profiles for BM vessels are shown in Fig. 6L and M. Similar to endothelial vessels, the secondary vessel's average velocity and wall shear stress were also higher than those of the primary vessel. The BM structure exhibited relatively lower velocity and shear stress compared to the corresponding endothelial vessels, primarily due to its wider tubular morphology. The site of the secondary vessel that underwent extensive thinning showed a step velocity and wall shear stress. In contrast, the primary vessel had a very gradual increase in velocity and wall shear stress. Our results confirmed that thinner vessels exhibit higher intraluminal velocity and shear stress than thicker ones, which is a well-established fluid dynamics principle. Next, we calculated the total volume flow rate of the BM and Endo structures. As expected, the thicker collagen structure had a higher flow rate (0.0748 μL s^{-1}) than the endothelial structure (0.04 μL s^{-1}).

The comparison of these two simulation results suggests that under high oscillatory shear stress, vessels experiencing abrupt changes in wall shear stress may begin to regress, possibly due to inadequate regulation of shear stress along the vessel. In contrast, when shear stress is evenly distributed, elevated levels may ultimately contribute to vessel stabilization, promoting the maturation of these vessels into primary arterioles.

Dopamine effect in vasodilation and vasoconstriction

Dopamine is a vaso-stimulant that has a dose-dependent effect on the cardiovascular system. It is a standard treatment for cardiac arrest and low blood pressure. A low dose of dopamine can induce vasodilation to increase blood flow, and a high dose can cause vasoconstriction.[41] To verify the functional response of the developed arteriole model, we exposed the vessels to different doses of dopamine to evaluate dose-dependent vasoconstriction or vasodilation. This experiment was repeated 4 times.

Fig. 7 shows one of the experimental results from introducing different dopamine concentrations into an AoC device with matured arterioles. The original arteriole network was first observed by flowing PBS mixed with 70 kDa FITC-labeled Dextran, as shown in Fig. 7A. Next, three different concentrations of dopamine, also mixed with FITC-labeled Dextran, were introduced into the arteriole network to investigate the vessels' response. The device was flushed with PBS between tests to allow the vessels to return to their initial state.

Fig. 7B–D show the experimental results of introducing 0.5 mg mL^{-1}, 1 mg mL^{-1}, and 2 mg mL^{-1} dopamine into the arteriole network. Note that the vessel structures at time 0 s were not as extensive as those in Fig. 7A. This was because the image shown in Fig. 7A had a longer incubation time, and FITC-labeled dextran can gradually diffuse into vessels that do not have an exit. This experimental study found that the arterioles were perfused with 0.5 mg mL^{-1} and 1 mg mL^{-1} dopamine but not with 2 mg mL^{-1} dopamine. To quantitatively analyze the vasodilation and vasoconstriction responses, we measured the vessel diameters at 0 s, 35 s, and 70 s after treatment. The vessel diameter (D_{time}) ratios of D_{35s}/D_{0s} and D_{70s}/D_{0s} were studied and

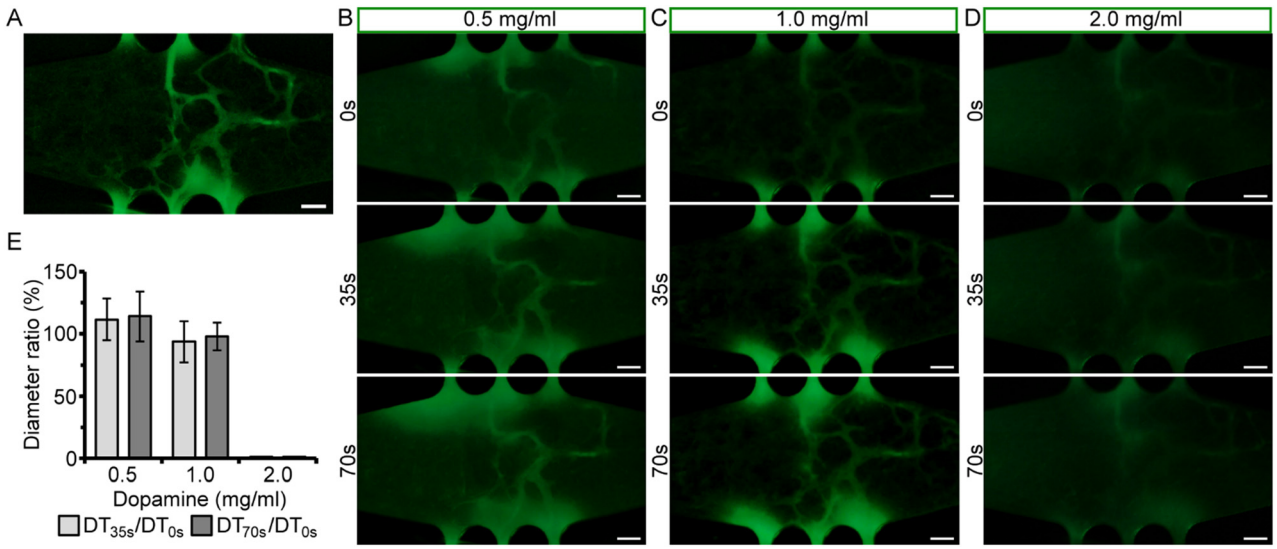

Fig. 7 Fluorescent micrographs of an arteriole network flowed with FITC-labeled dextran (A). Arteriole's response to 0.5 mg mL^{-1} (B), 1 mg mL^{-1} (C), and 2 mg mL^{-1} (D) dopamine at different time points. Analysis of vasodilation and vasoconstriction of the arteriole for applied dopamine dosage (E). 7 sections of the primary vessels were measured for quantification (scale bar = 100 μm).

Open Access Article. Published on 10 Juli 2025. Downloaded on 31.01.26 02:39:04.
This article is licensed under a Creative Commons Attribution 3.0 Unported Licence.

summarized in Fig. 7E. Secondary vessels that exhibited thinning or regression were excluded. Vasodilation was induced with 0.5 mg mL^{-1} dopamine, while vasoconstriction occurred with 2 mg mL^{-1} dopamine, resulting in almost no perfusion. The concentration of 1 mg mL^{-1} dopamine was the transitional concentration. The vasodilation response, transition state, and vasodilation response of another developed arteriole are also shown in the Videos S2† (2× speed video), which were sequentially treated with 0.5 mg mL^{-1}, 1 mg mL^{-1}, and 2 mg mL^{-1} dopamine. These experimental results confirm that the developed arterioles can be used to study drug effects on arterial vasodilation and vasoconstriction. They also suggest that the self-assembled arterioles mimic *in vitro* arterial functions.

Induction of arterial thrombosis

To verify the feasibility of using the AoC device for the arterial thrombosis study, we use PMA to stimulate the endothelium to release vWF. Once the injured endothelium releases vWF, it promotes blood clot formation by facilitating platelet adhesion, and arterial thrombosis can be studied. To observe this effect in the developed arterioles in the AoC device, we first stimulated the blood vessels by flowing 50 ng mL^{-1} PMA in EGM-2 media for 30 minutes. Next, the excess PMA was washed away with PBS, and whole human blood was flowed through the device for 1 hour. After flushing the blood from the AoC device, the arterioles were fixed for vWF and platelet (CD41a) immunostaining.

Fig. 8A and B show confocal and zoomed-in fluorescent images of induced thrombosis in developed arterioles using an AoC device, where nuclei, vWF, platelets, and collagen IV were stained in blue, green, red, and magenta. Fig. 8C to F show the individual fluorescent images of nuclei, vWF, BMs, and platelets.

We used the IMARIS surface function to highlight thrombosis formation and visualize their spatial correlations with BM and platelets, as shown in Fig. 8G. From Fig. 8B and G, it is evident that the HUAEC endothelium was successfully stimulated to release vWF, which was expressed in both the primary (white dashed lines) and secondary (light blue dashed lines) arterioles that remained perfused. In contrast, vWF wasn't released significantly in the control group, as shown in the supplementary Fig. S2.† These results demonstrated the efficiency of using PMA as an endothelial stimulant for releasing vWF. Furthermore, platelet accumulation was predominantly observed in the primary arterioles, suggesting maximal blood flow through these vessels. Fig. 8H shows a cross-sectional view of an induced thrombosis site, clearly illustrating platelet accumulation on top of the vWF-expressed area. The clot is situated within the luminal space of the arteriole. This result confirms that the current arteriole-on-a-chip model can be used to study arterial thrombosis, allowing for the observation and investigation of the role of vWF in thrombosis.

Discussion

In this study, we demonstrated that a self-assembled human arteriole network can be developed on a chip by sequentially stimulating vasculogenesis, angiogenesis, and arteriogenesis. The novelty of our design lies in the first-time use of primary HUAECs, HUSMCs, and NHLFs to develop an arteriolar network closely resembling *in vivo* architecture, as well as in studying dynamic vascular remodeling induced by the application of oscillatory flow to the developed arterioles.

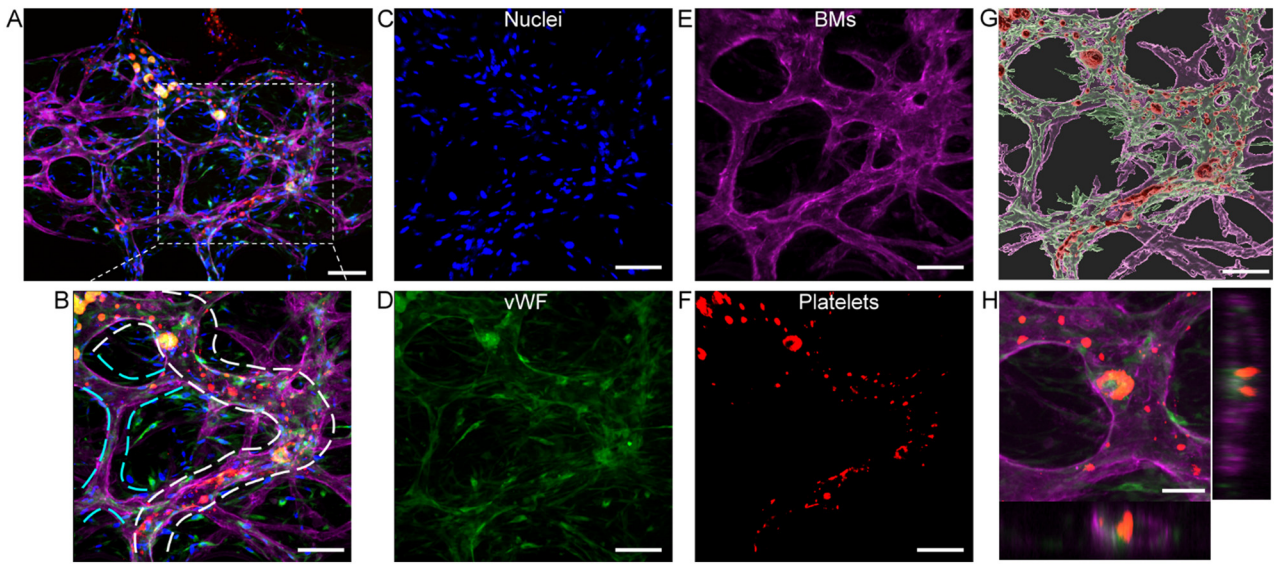

Fig. 8 Fluorescent micrographs showing an arteriole network following induction of arterial thrombosis (A and B), where (B) is an enlarged image of the white dashed box in (A). The nuclei, vWF, BMs and platelets were stained in blue (C), green (D), magenta (E), and red (F). IMARIS surface rendering showing vWF-mediated platelet trapping within the endothelium (G). A confocal image showing the location of the induced thrombosis (H) (scale bar = 100 μm (A–G), 50 μm (G and H))

This journal is © The Royal Society of Chemistry 2025

Open Access Article. Published on 10 Juli 2025. Downloaded on 31.01.26 02:39:04.
This article is licensed under a Creative Commons Attribution 3.0 Unported Licence.

While several studies have successfully developed self-assembled vascular networks and investigated the role of flow in vessel formation,[32,33,42–44] they have primarily focused on HUVEC-HLF co-cultures or tri-cultures involving brain endothelial cells, pericytes, and astrocytes. Notably, the interstitial flow in these models is static and occurs over millimeter-scale gradients. Our study employed vasculogenesis and angiogenesis to guide HUAECs, NHLFs, and HUSMCs into forming a perfused arteriolar network. To induce these two processes, the devices were driven by diffusion mass transport to create static and hypoxic conditions. This method followed the previously reported method in ref. 13. Briefly, the hypoxia in the AoC device was achieved by (i) using a cover glass to block gas exchange through the bottom surface, (ii) incorporating a thick PDMS top layer to limit oxygen diffusion from the environment,[45] (iii) placing the device in a 5% O_2 incubator, and (iv) the arteriole chamber was made much larger than the 100 μm O_2 diffusion limit. As a result, oxygen was primarily supplied *via* the two side channels. Since the chamber size exceeded the O_2 diffusion limit, hypoxia can be effectively created in the arteriole chamber's central region.

Our study demonstrated that arteriogenesis can be stimulated by applying continuous oscillatory flow to the perfused vessels, which increased intraluminal wall shear stress. The resulting arterioles mimicked human arteriole structure with HUAEC endothelium enveloped by a layer of SMCs and outer BM (Fig. 3L). Note that the arteriogenic process observed in our study contrasts with previously reported interstitial flow-driven HMVEC vessel growth, which relied on convective flow within the interstitial space.[29–31] The wall shear stress we applied to the developed arterioles was 3 orders higher than the interstitial flow. The elevated shear stress subsequently promoted the development and maturation of the vascular network.

Our studies also demonstrated a direct correlation between the magnitude of applied wall shear stress and the extent of vessel remodeling, highlighting the critical role of hemodynamic forces in vascular adaptation. When a low shear stress (~83 Pa) is applied, the vascular network shows extensive remodeling characterized by an increased number of perfused vessel segments (Fig. 4B) without a significant change in vessel diameter. Interestingly, low oscillating pressure also facilitated the perfusion of previously non-perfused vessels, underscoring the critical role of shear stress in promoting vessel perfusion, as shown in the Fig. S3.†

Upon application of high oscillating shear stress, the vascular networks exhibited both extensive and regressive remodeling for the first 24 hours, characterized by a significant increase in the diameter of larger vessels and the regression of smaller vessels. Over the subsequent 24 hours, only a marginal increase in vessel diameter was observed, although regression of secondary vessels continued (Fig. 4I and J). This result highlights the temporal influence of a specific shear stress range on vascular remodeling. The abrupt onset of high shear stress induced rapid network remodeling for the first 24 hours, after which the vessel architecture remodeled as the hydrodynamic and metabolic environments stabilized. Therefore, the enlargement of the primary vessel at the second 24 hours was not as extensive as that of the first 24 hours. We hypothesize that further increases in shear stress to the physiological level of arteriogenesis will promote additional vessel enlargement and remodeling to remodel the network again to accommodate the applied hemodynamic forces. The secondary vessel could eventually regress or become a shunt vessel. Furthermore, our observations also agree well with previously reported animal studies on the effect of wall shear stress on vascular remodeling. In fact, Clark demonstrated in a frog model that small blood vessels regress after a decrease in flow rate, and vessels exposed to high shear stress are stabilized.[46] Thus, our AoC device and experimental studies provide an initial framework for studying continuous shear stress-mediated arteriogenesis and lay the groundwork for future investigations into optimizing oscillating shear stress to enhance arteriole network formation.

Comparison of stained devices across all three conditions revealed distinct differences in vessel architecture due to the variations in applied shear stress (Fig. 3). Higher shear stress promoted greater co-localization of SMCs and HUAECs, accompanied by the formation of larger and better-perfused vessels. Notably, the high shear (HS) condition exhibited the highest SMC proliferation and extensive wrapping around the endothelium. In contrast, the static condition showed minimal SMC association with vessels, while the low shear stress condition demonstrated intermediate SMC co-localization. These findings underscore the critical role of wall shear stress in promoting arteriole-like structure formation, which could not be achieved under a static physiological environment.

As previously discussed, the presence of empty basement membranes without endothelium indicates regressed blood vessels. Animal studies have shown that these structures indicate the existence of a prior vascular network, appearing post-regression.[47,48] This suggests that the basement membrane retains a blueprint of the initial vasculature formed during vasculogenesis and angiogenesis, which is subsequently remodeled in response to external and internal stimuli. Our study shows that the retention of initial vessel architecture depends on the magnitude of applied shear stress. Vessel diameter showed the greatest reduction under static conditions, with vessel diameters decreasing by 30.43% and 35% in static and LS conditions, compared to only 15.62% in the HS condition. The final vessel coverage relative to the BM area was markedly reduced in static (74.24%) and LS (64.19%) conditions, while HS showed only a 30.37% reduction. This result suggests that extensive regressions occurred in static and LS conditions. The difference between the significantly larger vessel area and much smaller vessel and BM area in the HS condition underscores the importance of introducing a high oscillatory shear stress to maintain arteriolar structure and stability.

Open Access Article. Published on 10 Juli 2025. Downloaded on 31.01.26 02:39:04.
This article is licensed under a Creative Commons Attribution 3.0 Unported Licence.

The experimental result in Fig. 6A demonstrated that applying a high shear stress to the vessel wall can guide the HUAEC vessels to develop into a primary vessel and the others into secondary vessels. To infer the hydrodynamic environment of the HUAEC vessels before and after the induction of the high wall shear stress, finite element analysis was conducted for the endothelium (Endo; Fig. 6D, F and H) and basement membrane (BM; Fig. 6E, G and I). Simulated wall shear stresses revealed that secondary vessels exhibited higher wall shear stress and an abrupt shear stress than primary vessels (Fig. 6L and M). This suggests that fluid preferentially flowed through vessels with a lower shear stress level and gradient, promoting their development into primary vessels, while areas exposed to higher shear stress formed secondary vessels. Furthermore, the region with the highest wall shear stress, identified at location '*a*', likely marks the onset of secondary vessel regression in Fig. 6F and G. The level of wall shear stress for vessels was between 1.42 Pa and 8.13 Pa. This level of wall shear stress matches well with the 0.5 Pa to 1 Pa of the aorta and conduit arteries and 5.2 Pa of the arterioles, suggesting that the present method can properly simulate the *in vivo* physiological environment of arteries.[49] Notably, the wall shear stress at the basement membrane was approximately five times lower than at the endothelium. This difference is attributed to the presence of an intermediate SMC layer, which increased the overall vessel diameter. Despite this, the shear stress distribution still reflects the hydrodynamic environment of the original vessel structure.

To check if the remodeling process is unique to arterial endothelial cells and smooth muscle cells, we also studied the co-culture of HUAECs + NHLFs and HUVECs + NHLFs, as shown in supplementary Fig. S4A and B,† respectively. We found a similar vessel remodeling process in the HUAECs + NHLFs model under high-shear stress conditions. Primary vessels were enlarged, and the secondary vessel regression persisted for 72 hours. In contrast, vessels developed in the HUVECs + NHLFs model showed a lower level of vessel remodeling under high-shear stress conditions. As shown in Fig. S5,† vessel diameter analysis revealed a significant increase in the HUAECs + NHLFs group over the first 48 hours of shear stress. Specifically, HUAEC vessel diameters increased by 31.5% at 24 hours and 24% at 48 hours, with only marginal, statistically insignificant changes observed thereafter. In contrast, the HUVEC + NHLF group exhibited a significant diameter increase only within the first 24 hours, with no notable changes over the following 48 hours. Notably, the HUVEC vessels exhibited only a 16% diameter increase within the first 24 hours, approximately half the enlargement observed in HUAEC vessels. This indicates that HUAECs may have a greater capacity to adapt to shear stress through vessel enlargement. Also, high-shear stress could be a unique physiological cue for the arterial remodeling process, and the endothelium is responsible for sensing and responding to these sudden changes in a physiological environment.

The observations of the extensive arteriogenic remodeling process found in the HUAECs + HUSMCs + NHLFs and HUAECs + NHLFs co-culture system, but not for the HUVECs + NHLFs case. These results suggest that the arterial endothelial cells could have a unique gene expression over the capillary and venous endothelial cells, and that they can respond to the high oscillatory shear stress and start the arteriogenesis to compensate for arterial injury. Furthermore, the technique to develop iPSC-derived ECs has become very mature in recent years. It is postulated that the iPSC-derived ECs that have similar gene expression to the primary arterial ECs could potentially express the arteriogenic remodeling process. An extensive study is needed to verify this hypothesis by using different arterial endotherlial cells from different organs and identifying the gene expressions.

These experimental findings also suggest that arterial remodeling and arterial functionality are two different behaviors of arteries. The remodeling process is part of vessel development, whereas the arterial function depends on both the endothelium and the smooth muscle layer. The arteriole structure stabilized once their hydrodynamic and metabolic environment reached a steady state, and the remodeling activities became quiescent. The arteriole-like functions of the developed arteriole vessels depend on the signaling and coordination between the developed endothelium and the smooth muscle layer. We validated the functional responsiveness of the developed arterioles by treating them with different dosages of dopamine. Prior studies have shown that vasomotion, the active regulation of vessel diameter, is a defining characteristic of arteries and is primarily governed by the SMC layer.[50–53] Vasodilators are used to lower blood pressure and manage conditions like acute heart failure, myocardial infarction, and chronic congestive heart failure, while vasoconstrictors are applied in treating hypothermia, shock, asthma, and COPD. Dopamine can be used as both a vasodilator and a vasoconstrictor, depending on its dosage. However, the effect of dopamine on ECs is poorly understood. Previous studies have reported that dopamine disrupts endothelial function, reduces nitric oxide (NO) production, and compromises cell junctions.[54,55] However, the dose-dependent effect on fluid flow is underexplored. We investigated how dopamine affects vascular function using two engineered vessel types: one incorporating smooth muscle cells (SMCs) and one without them. By perfusing different concentrations of dopamine through these networks, we observed distinct responses. At low (0.5 mg mL^{-1}) and intermediate (1 mg mL^{-1}) concentrations, both vessel types maintained perfusability (Video-S2 and S3†). However, only the SMC-containing vessels exhibited vasodilation, highlighting the active role of SMCs in vessel response. At a higher dopamine dose (2 mg mL^{-1}), the SMC co-cultured vessels contracted significantly but didn't occlude completely. Yet, the vessels became imperfusable within few seconds. Notably, even in the absence of SMCs, vessels also lost perfusion shortly after dopamine exposure, despite no

 This journal is © The Royal Society of Chemistry 2025

Open Access Article. Published on 10 Juli 2025. Downloaded on 31.01.26 02:39:04.
This article is licensed under a Creative Commons Attribution 3.0 Unported Licence.

substantial changes in diameter (Video-S3†). These observations, in line with previous reports, indicate that dopamine-induced changes in vessel perfusability are dose-dependent and primarily mediated by the endothelial cells. At elevated concentrations, dopamine may compromise the integrity of the endothelial barrier, leading to impaired perfusion. Collectively, the results emphasize that vasomotion is mediated by SMCs, while endothelial cells primarily regulate vessel perfusability. These findings further demonstrate the AoC platform's ability to dissect cell-type-specific responses to drugs and serve as a powerful tool for evaluating vascular toxicity and informing therapeutic strategies.

Thrombosis is the abnormal formation of a blood clot within a vessel, which can obstruct circulation and lead to life-threatening complications. However, the mechanisms of arterial thrombosis, venous thrombosis, and microvascular thrombosis are different. A comprehensive review of their differences can be found in ref. 56. Currently, most of the reported vessel-on-a-chip models utilize HUVECs or HMVECs. They are either lined in an artificial microchannel[57,58] or on a porous membrane with SMCs lining on the opposite side of the membrane.[59] However, the cellular responses of arterial endothelial cells can differ from those of endothelial cells in microvasculatures and veins. Arterial thrombosis often arises from atherosclerosis, an inflammatory condition marked by disrupted vasoconstriction–vasodilation balance and increased vascular permeability to lipoproteins. In response, smooth muscle cells migrate into the intimal layer, proliferate, resist apoptosis, and promote extracellular matrix buildup and lipid accumulation, leading to arterial wall thickening and narrowing of the lumen.[60] Thus, to study atherosclerosis and arterial thrombosis, it is important to reconstruct the anatomical structure of the arteries. In this study, we successfully induced arterial thrombosis in a self-assembled arteriole model. While the underlying mechanisms were not explored, this platform offers a foundation to study endothelial–SMC interactions and develop targeted therapies.

Conclusion

In this paper, we report a physiological approach to develop the first self-assembled human arteriole network in a microfluidic device using HUAECs, HUSMCs, and NHLFs. We applied the concept of the analogy between microfluidic channels and resistive circuits to control the physiological environment inside the 3-D arteriole chamber of the AoC device. A hypoxic environment was first induced to stimulate vasculogenesis and angiogenesis to form a connected vascular network. Then, 1 Hz oscillating pressure was introduced to the luminal space of developed vessels for stimulating arteriogenesis. Our results demonstrate that cyclic fluid shear stress is an important physiological cue and regulator of artery development, including perfusability, arterial remodeling, and co-localization of arterial endothelial cells and smooth muscle cells. Furthermore, our study suggests that wall shear stress is an important factor in maturing arterial vessels, and the level of wall shear stress should be physiologically relevant to mimic the *in vivo* environment. Finally, we verify that this arteriole-on-a-chip model can be an *in vitro* model for developing arterial-related diseases. Vasodilation and vasoconstriction can be induced on the chip, and whole human blood can directly flow into the arteriole network to study arterial thrombosis. In conclusion, our study presents a novel method for developing an arteriole model on a chip. It can potentially replace animal models for artery-related cardiovascular disease studies, which meets the replacement concept of the current 3Rs trends for drug discovery and development.

Data availability

All data associated with this study are present in the paper and the ESI† document. Raw data that support this study are available from the corresponding authors upon reasonable request.

Author contributions

Y.-H. Hsu – conceptualization, supervision, funding acquisition, project administration, methodology, investigation, writing – review & editing; S. Shivani – original draft, formal analysis, visualization, investigation, validation; H. J. Wang & Y. T. Chen, formal analysis, visualization, investigation, validation; C. T. Lin – supervision, writing – review & editing.

Conflicts of interest

There are no conflicts to declare.

Acknowledgements

This work was supported by the National Science and Technology Council, Taiwan (R.O.C) (MOST 109-2221-E-002-045- and MOST 111-2221-E-002-036-MY3).

References

1 D. Soto Veliz, K. Lin and C. Sahlgren, *Smart Med.*, 2023, **2**, e20220030, DOI: **10.1002/SMMD.20220030**.
2 M. Vaduganathan, G. A. Mensah, J. V. Turco, V. Fuster and G. A. Roth, *J. Am. Coll. Cardiol.*, 2022, **80**, 2361–2371, DOI: **10.1016/j.jacc.2022.11.005**.
3 S. Zhang, Z. Wan and R. D. Kamm, *Lab Chip*, 2021, **21**, 473–488, DOI: **10.1039/d0lc01186j**.
4 A. Fritschen and A. Blaeser, *Biomaterials*, 2021, **268**, 120556, DOI: **10.1016/j.biomaterials.2020.120556**.
5 Z. Xu, E. Li, Z. Guo, R. Yu, H. Hao, Y. Xu, Z. Sun, X. Li, J. Lyu and Q. Wang, *ACS Appl. Mater. Interfaces*, 2016, **8**, 25840–25847, DOI: **10.1021/acsami.6b08746**.

Open Access Article. Published on 10 Juli 2025. Downloaded on 31.01.26 02:39:04.
This article is licensed under a Creative Commons Attribution 3.0 Unported Licence.

6 L. Wang, Z.-L. Zhang, J. Wdzieczak-Bakala, D.-W. Pang, J. Liu and Y. Chen, *Lab Chip*, 2011, **11**, 4235, DOI: **10.1039/c1lc20722a**.
7 B. M. Baker, B. Trappmann, S. C. Stapleton, E. Toro and C. S. Chen, *Lab Chip*, 2013, **13**, 3246, DOI: **10.1039/c3lc50493j**.
8 D.-H. T. Nguyen, S. C. Stapleton, M. T. Yang, S. S. Cha, C. K. Choi, P. A. Galie and C. S. Chen, *Proc. Natl. Acad. Sci. U. S. A.*, 2013, **110**, 6712–6717, DOI: **10.1073/pnas.1221526110**.
9 L. L. Bischel, E. W. K. Young, B. R. Mader and D. J. Beebe, *Biomaterials*, 2013, **34**, 1471–1477, DOI: **10.1016/j.biomaterials.2012.11.005**.
10 A. D. Van Der Meer, V. V. Orlova, P. Ten Dijke, A. Van Den Berg and C. L. Mummery, *Lab Chip*, 2013, **13**, 3562, DOI: **10.1039/c3lc50435b**.
11 Y.-H. Hsu, W.-C. Yang, Y.-T. Chen, C.-Y. Lin, C.-F. Yang, W.-W. Liu, S. Shivani and P.-C. Li, *Lab Chip*, 2024, **24**, 2644–2657, DOI: **10.1039/d3lc00891f**.
12 J. Paek, S. E. Park, Q. Lu, K.-T. Park, M. Cho, J. M. Oh, K. W. Kwon, Y. Yi, J. W. Song, H. I. Edelstein, J. Ishibashi, W. Yang, J. W. Myerson, R. Y. Kiseleva, P. Aprelev, E. D. Hood, D. Stambolian, P. Seale, V. R. Muzykantov and D. Huh, *ACS Nano*, 2019, **13**, 7627–7643, DOI: **10.1021/acsnano.9b00686**.
13 Y.-H. Hsu, M. L. Moya, P. Abiri, C. C. W. Hughes, S. C. George and A. P. Lee, *Lab Chip*, 2013, **13**, 81–89, DOI: **10.1039/c2lc40787f**.
14 M. L. Moya, Y.-H. Hsu, A. P. Lee, C. C. W. Hughes and S. C. George, *Tissue Eng., Part C*, 2013, **19**, 730–737, DOI: **10.1089/ten.tec.2012.0430**.
15 S. Kim, H. Lee, M. Chung and N. L. Jeon, *Lab Chip*, 2013, **13**, 1489, DOI: **10.1039/c3lc41320a**.
16 C. Kim, J. Kasuya, J. Jeon, S. Chung and R. D. Kamm, *Lab Chip*, 2015, **15**, 301–310, DOI: **10.1039/c4lc00866a**.
17 E. Hirth, W. Cao, M. Peltonen, E. Kapetanovic, C. Dietsche, S. Svanberg, M. Filippova, S. Reddy and P. S. Dittrich, *Lab Chip*, 2024, **24**, 292–304, DOI: **10.1039/d3lc00719g**.
18 M. L. Ewald, A. P. Lee, Y. H. Chen and C. C. W. Hughes, *Lab Chip*, 2021, **21**, 3244–3262, DOI: **10.1039/d1lc00530h**.
19 L. Niklason and G. Dai, *Annu. Rev. Biomed. Eng.*, 2018, **20**, 431–447, DOI: **10.1146/annurev-bioeng-062117-121231**.
20 E. Trimm and K. Red-Horse, *Nat. Rev. Cardiol.*, 2023, **20**, 197–210, DOI: **10.1038/s41569-022-00770-1**.
21 N. G. Dela Paz and P. A. D'Amore, *Cell Tissue Res.*, 2009, **335**, 5–16, DOI: **10.1007/s00441-008-0706-5**.
22 A. Günther, S. Yasotharan, A. Vagaon, C. Lochovsky, S. Pinto, J. Yang, C. Lau, J. Voigtlaender-Bolz and S.-S. Bolz, *Lab Chip*, 2010, **10**, 2341, DOI: **10.1039/c004675b**.
23 S. Yasotharan, S. Pinto, J. G. Sled, S.-S. Bolz and A. Günther, *Lab Chip*, 2015, **15**, 2660–2669, DOI: **10.1039/c5lc00021a**.
24 A. Tan, K. Fujisawa, Y. Yukawa and Y. T. Matsunaga, *Biomater. Sci.*, 2016, **4**, 1503–1514, DOI: **10.1039/c6bm00340k**.
25 E. Hirth, W. Cao, M. Peltonen, E. Kapetanovic, C. Dietsche, S. Svanberg, M. Filippova, S. Reddy and P. S. Dittrich, *Lab Chip*, 2024, **24**, 292–304, DOI: **10.1039/d3lc00719g**.
26 C. Su, N. V. Menon, X. Xu, Y. R. Teo, H. Cao, R. Dalan, C. Y. Tay and H. W. Hou, *Lab Chip*, 2021, **21**, 2359–2371, DOI: **10.1039/d1lc00131k**.
27 V. Paloschi, J. Pauli, G. Winski, Z. Wu, Z. Li, L. Botti, S. Meucci, P. Conti, F. Rogowitz, N. Glukha, N. Hummel, A. Busch, E. Chernogubova, H. Jin, N. Sachs, H. Eckstein, A. Dueck, R. A. Boon, A. R. Bausch and L. Maegdefessel, *Adv. Healthcare Mater.*, 2024, **13**, 2302907, DOI: **10.1002/adhm.202302907**.
28 N. C. A. Van Engeland, A. M. A. O. Pollet, J. M. J. Den Toonder, C. V. C. Bouten, O. M. J. A. Stassen and C. M. Sahlgren, *Lab Chip*, 2018, **18**, 1607–1620, DOI: **10.1039/c8lc00286j**.
29 M. Heil, I. Eitenmüller, T. Schmitz-Rixen and W. Schaper, *J. Cell. Mol. Med.*, 2006, **10**, 45–55, DOI: **10.1111/j.1582-4934.2006.tb00290.x**.
30 I. Buschmann and W. Schaper, *Physiology*, 1999, **14**, 121–125, DOI: **10.1152/physiologyonline.1999.14.3.121**.
31 M. A. Winkelman, D. Y. Kim, S. Kakarla, A. Grath, N. Silvia and G. Dai, *Lab Chip*, 2022, **22**, 170–192, DOI: **10.1039/d1lc00605c**.
32 M. A. Winkelman, D. Y. Kim, S. Kakarla, A. Grath, N. Silvia and G. Dai, *Lab Chip*, 2022, **22**, 170–192, DOI: **10.1039/d1lc00605c**.
33 H. Sano, M. Watanabe, T. Yamashita, K. Tanishita and R. Sudo, *Biofabrication*, 2020, **12**, 045008, DOI: **10.1088/1758-5090/ab9316**.
34 P. A. Galie, D. H. T. Nguyenc, C. K. Choia, D. M. Cohena, P. A. Janmeyb and C. S. Chena, *Proc. Natl. Acad. Sci. U. S. A.*, 2014, **111**, 7968–7973, DOI: **10.1073/pnas.1310842111**.
35 K. W. Oh, K. Lee, B. Ahn and E. P. Furlani, *Lab Chip*, 2012, **12**, 515–545, DOI: **10.1039/c2lc20799k**.
36 J. Sonne, A. Goyal and W. Lopez-Ojeda, Dopamine, *StatPearls*, StatPearls Publishing, Treasure Island, FL, 2024.
37 Thrombosis and Embolism: from Research to Clinical Practice: Volume 1, *Advances in Experimental Medicine and Biology vol. 906*, ed. Md. S. Islam, Springer International Publishing, AG Switzerland, 2017DOI: **10.1007/978-3-319-22108-3**.
38 S. Krishnamurthi, S. Joseph and V. Kakkar, *Biochim. Biophys. Acta, Mol. Cell Res.*, 1987, **927**, 429–436, DOI: **10.1016/0167-4889(87)90109-1**.
39 J. C. Giddings and L. Shall, *Thromb. Res.*, 1987, **47**, 259–267, DOI: **10.1016/0049-3848(87)90139-3**.
40 R. Vracko, *Am. J. Pathol.*, 1974, **77**, 313–346.
41 R. Suzuki, S. Uchino, Y. Sasabuchi, A. Kawarai Lefor and M. Sanui, *Crit. Care*, 2022, **26**, 90, DOI: **10.1186/s13054-022-03960-y**.
42 M. Campisi, Y. Shin, T. Osaki, C. Hajal, V. Chiono and R. D. Kamm, *Biomaterials*, 2018, **180**, 117–129, DOI: **10.1016/j.biomaterials.2018.07.014**.
43 A. Blazeski, M. A. Floryan, Y. Zhang, O. R. Fajardo Ramírez, E. Meibalan, J. Ortiz-Urbina, E. Angelidakis, S. E. Shelton, R. D. Kamm and G. García-Cardeña, *Biomaterials*, 2024, **311**, 122686, DOI: **10.1016/j.biomaterials.2024.122686**.

This journal is © The Royal Society of Chemistry 2025

Open Access Article. Published on 10 Juli 2025. Downloaded on 31.01.26 02:39:04.
This article is licensed under a Creative Commons Attribution 3.0 Unported Licence.

44 S. Zhang, Z. Wan, G. Pavlou, A. X. Zhong, L. Xu and R. D. Kamm, *Adv. Funct. Mater.*, 2022, **32**, 2206767, DOI: **10.1002/adfm.202206767**.
45 M. E. Cox and B. Dunn, *J. Polym. Sci., Part A:Polym. Chem.*, 1986, **24**, 621–636, DOI: **10.1002/pola.1986.080240405**.
46 E. R. Clark, *Am. J. Anat.*, 1918, **23**, 37–88, DOI: **10.1002/aja.1000230103**.
47 T. Inai, M. Mancuso, H. Hashizume, F. Baffert, A. Haskell, P. Baluk, D. D. Hu-Lowe, D. R. Shalinsky, G. Thurston, G. D. Yancopoulos and D. M. McDonald, *Am. J. Pathol.*, 2004, **165**, 35–52, DOI: **10.1016/S0002-9440(10)63273-7**.
48 B. Sennino, B. L. Falcón, D. McCauley, T. Le, T. McCauley, J. C. Kurz, A. Haskell, D. M. Epstein and D. M. McDonald, *Cancer Res.*, 2007, **67**, 7358–7367, DOI: **10.1158/0008-5472.CAN-07-0293**.
49 T. G. Papaioannou and C. Stefanadis, *Hellenic J. Cardiol.*, 2005, **46**, 9–15.
50 C. Aalkjær and H. Nilsson, *Br. J. Pharmacol.*, 2005, **144**, 605–616, DOI: **10.1038/sj.bjp.0706084**.
51 M. Lamboley, A. Schuster, J.-L. Bény and J.-J. Meister, *Am. J. Physiol.*, 2003, **285**, H562–H569, DOI: **10.1152/ajpheart.00526.2002**.
52 B. Khalil, A. Rosani and S. J. Warrington, in *StatPearls*, StatPearls Publishing, Treasure Island, FL, 2025.
53 I. Armando, V. A. M. Villar and P. A. Jose, *Compr. Physiol.*, 2011, **1**, 1075–1117, DOI: **10.1002/cphy.c100032**.
54 Y. Hao, Y. Su, Y. He, W. Zhang, Y. Liu, Y. Guo, X. Chen, C. Liu, S. Han, B. Wang, Y. Liu, W. Zhao, L. Mu, J. Wang, H. Peng, J. Han and Q. Kong, *J. Neuroinflammation*, 2024, **21**, 10, DOI: **10.1186/s12974-023-03005-3**.
55 Z. Yang, Y. Li, M. Huang, X. Li, X. Fan, C. Yan, Z. Meng, B. Liao, N. Hamdani, X. Yang, X. Zhou, I. El-Battrawy and I. Akin, *Int. J. Med. Sci.*, 2024, **21**, 1964–1975, DOI: **10.7150/ijms.96550**.
56 N. K. R. Pandian, R. G. Mannino, W. A. Lam and A. Jain, *Curr. Opin. Biomed. Eng.*, 2018, **5**, 29–34, DOI: **10.1016/j.cobme.2017.12.001**.
57 J. Berry, F. J. Peaudecerf, N. A. Masters, K. B. Neeves, R. E. Goldstein and M. T. Harper, *Lab Chip*, 2021, **21**, 4104–4117, DOI: **10.1039/d1lc00347j**.
58 Y. Zheng, J. Chen, M. Craven, N. W. Choi, S. Totorica, A. Diaz-Santana, P. Kermani, B. Hempstead, C. Fischbach-Teschl, J. A. López and A. D. Stroock, *Proc. Natl. Acad. Sci. U. S. A.*, 2012, **109**, 9342–9347, DOI: **10.1073/pnas.1201240109**.
59 A. Jain, R. Barrile, A. Van Der Meer, A. Mammoto, T. Mammoto, K. De Ceunynck, O. Aisiku, M. Otieno, C. Louden, G. Hamilton, R. Flaumenhaft and D. Ingber, *Clin. Pharmacol. Ther.*, 2018, **103**, 332–340, DOI: **10.1002/cpt.742**.
60 R. Ross and J. A. Glomset, *Science*, 1973, **180**, 1332–1339, DOI: **10.1126/science.180.4093.1332**.